

1 **Nucleation and growth of sub-3 nm particles in the polluted urban atmosphere of a megacity in**
2 **China**

3 Huan Yu^{1,2,*}, Luyu Zhou¹, Liang Dai¹, Wenchao Shen¹, Jun Zheng^{1,2}, Yan Ma^{1,2}, Mindong Chen^{1,2}

4 1. School of Environmental Science and Engineering, Nanjing University of Information Science and
5 Technology, Nanjing, China

6 2. Collaborative Innovation Center of Atmospheric Environment and Equipment Technology,
7 Nanjing University of Information Science and Technology, Nanjing, China

8

9 Corresponding authors: hyu@nuist.edu.cn

10

11 **Abstract**

12 Particle size distribution down to 1.4 nm was measured in the urban atmosphere of Nanjing, China in
13 spring, summer and winter during 2014-2015. Sub-3 nm particle event, which is equivalent to
14 nucleation event, occurred on 42 out of total 90 observation days, but new particles could grow to
15 cloud condensation nuclei (CCN)-active sizes on only 9 days. In summer, infrequent nucleation was
16 limited by both unfavorable meteorological conditions (high temperature and RH) and reduced
17 anthropogenic precursor availability due to strict emission control measures during the 2014 Youth
18 Olympic Games in Nanjing. The limiting factors for nucleation in winter and spring were
19 meteorological conditions (radiation, temperature, and RH) and condensation sink, but for the further

20 growth of sub-3 nm particles to CCN-active sizes, anthropogenic precursors again became limiting
21 factors. Nucleation events were strong in the polluted urban atmosphere. Initial $J_{1.4}$ at the onset and
22 peak $J_{1.4}$ at the noontime could be up to $2.1 \times 10^2 \text{ cm}^{-3} \text{ s}^{-1}$ and $2.5 \times 10^3 \text{ cm}^{-3} \text{ s}^{-1}$, respectively, during the
23 8 nucleation events selected from different seasons. Time-dependent $J_{1.4}$ usually showed good linear
24 correlations with a sulfuric acid proxy for every single event ($R^2 = 0.56 - 0.86$, excluding a day with
25 significant nocturnal nucleation), but the correlation among all the 8 events deteriorated ($R^2 = 0.17$)
26 due to temperature or season change. We observed that new particle growth rate (GR) did not
27 increase monotonically with particle size, but had a local maximum up to 25 nm h^{-1} between 1-3 nm.
28 The existence of local maxima GR in sub-3 nm size range, though highly sensitive to measurement
29 uncertainties, is potentially real and might give new insight into cluster dynamics in polluted
30 environments. In this study such growth rate behavior was interpreted as the solvation effect of
31 organic activating vapor in newly formed inorganic nuclei.

32

33 1. Introduction

34 New particle formation (NPF) is an important source of secondary aerosols in the atmosphere
35 (Kulmala et al., 2004a). Field studies and model simulations have consistently shown that NPF can
36 enhance cloud condensation nuclei (CCN) concentrations and contribute significantly to the global
37 CCN production (Wiedensohler et al., 2009; Yue et al., 2011; Spracklen et al., 2008; Pierce and
38 Adams, 2009; Merikanto, 2009; Yu and Luo, 2009; Matsui et al. 2013). NPF is a two-stage process
39 consisting of formation of clusters and subsequent growth to detectable sizes (Kulmala et al., 2000).
40 Recently, chamber experiments have made substantial progress in revealing the fundamental

41 processes involved in particle nucleation and growth (Kirkby et al., 2011; Almeida et al., 2013;
42 Schobesberger et al., 2013; Riccobono et al., 2014; Ehn et al., 2014; Kürten et al., 2014). However,
43 consistent theories are still under investigation to quantify the processes physically, chemically, and
44 dynamically (Kulmala et al., 2013, 2014). For example, the identity and physico-chemical properties
45 of assisting vapors other than sulfuric acid (H_2SO_4) are uncertain so far. It is also uncertain what
46 mechanisms allow the assisting vapors to overcome strong Kelvin effect over sub-3 nm particles.
47 Existing mechanisms include condensation of extremely low volatility organic compounds (Ehn et
48 al., 2014), nano-Köhler activation (Kulmala et al., 2004b), heterogeneous chemical reactions (Zhang
49 and Wexler, 2002), heterogeneous nucleation (Wang et al., 2013), and adsorption of organics on
50 cluster surface (Wang and Wexler, 2013). However, the relative importance of various mechanisms
51 is unknown.

52 Direct measurements of size- and time dependent nucleation rate and growth rate in sub-3 nm
53 size range are important to constrain the relative contributions from different mechanisms and
54 precursors. Such measurements are also important to evaluate the survival probability of new particle
55 to CCN-active sizes (~100 nm for soluble particles at 0.2% super saturation, Pierce and Adams, 2009)
56 and to reveal the limiting factors in the process. Recently, a series of new instruments have been
57 developed to measure sub-3 nm aerosol number concentration and chemical composition, such as
58 condensation particle counters (e.g., PSM, DEG-SMPS, Jiang et al., 2011a; Sipila et al., 2009;
59 Vanhanen et al., 2011), ion spectrometers (e.g., NAIS, Asmi et al., 2009), and mass spectrometers
60 (e.g., Cluster-CIMS, APi-TOF, CI-APi-TOF, Jokinen et al., 2012; Junninen et al., 2010; Zhao et al.,
61 2010). Kuang et al. (2012) developed a de-coupling method to measure size- and time dependent

62 growth rates of sub-5 nm particles. Their results at two urban sites in U.S.A showed that
63 size-resolved growth rates increased approximately linearly with particle size from 1 to 5 nm.
64 Similar results were also observed in the Boreal forest (Kulmala et al., 2013; Lehtipalo et al., 2014).
65 Based on growth rates measured below 2 nm, Kulmala et al. (2013) identified three separate size
66 regimes, which were dominated by different key gas to particle conversion processes.

67 The relative contribution of different precursors and mechanisms to the nucleation and growth of
68 1-3 nm particles may vary greatly with atmospheric conditions (Riipinen et al., 2012). Therefore,
69 sub-3 nm particle measurements in a variety of atmospheric conditions, e.g., remote or urban
70 atmosphere, biogenic- or anthropogenic emission dominated areas, are immensely valuable.
71 Unfortunately, such data are very sparse until now (Jiang et al., 2011b; Kuang et al., 2012; Kulmala
72 et al., 2013; Lehtipalo et al., 2009, 2010, 2011; Yu et al., 2014a, b). China is suffering from severe
73 atmospheric particulate matter pollution in recent years (Chan and Yao, 2008; Yue et al., 2011). To
74 the best of our knowledge, only two studies were conducted in China to measure the occurrence of
75 new particles down to ~1 nm. In these two studies, air ions (Herrmann et al., 2014) or neutral
76 particles (Xiao et al., 2015) were measured by AIS or PSM in two urban locations of Yangtze River
77 Delta (YRD) region. Both studies were conducted in the winter season.

78 Here we reported the nucleation and growth of sub-3 nm particles in the urban atmosphere of
79 Nanjing, China on arbitrarily selected observation days in spring, summer and winter of 2014-2015.
80 Our aim was to (1) provide new information about the initial steps of NPF based on size- and time
81 resolved nucleation rate and growth rate measurements, and (2) find possible limiting factors behind
82 the seasonal and diurnal variations of nucleation events in the polluted urban atmosphere.

83 2. Methodology

84 2.1 Field measurements

85 Nanjing is the second largest megacity after Shanghai in the YRD region of China (Chan and
86 Yao, 2008). The YRD city cluster, covering 2.1×10^5 km² land with 170 million residents, is one of
87 the most populated and industrialized regions in China. Field measurement was conducted from the
88 third floor (15m above the ground level) of an academic building beside a Chinese national
89 meteorology observatory facility in NUIST campus (32.20° N, 118.71° E, symbol ① in Figure 1).
90 The sampling was carried out during the months of May (May 10-30, 2014), June (June 1-15, 2014),
91 December (December 24-31, 2014), February (February 16-22, 2015), and March (March 1-7, 2015).
92 Total 58 measurement days were arbitrarily selected to represent spring, early summer and winter
93 seasons, but to avoid any rain-event.

94 As part of an intensive summer campaign (12 August-12 September 2014), the summer
95 measurement was conducted at a local governmental meteorology observatory platform (32.06°N,
96 118.70°E) that is 14km south to the NUIST site (② in Figure 1). The instruments were housed in an
97 air conditioned trailer, using exactly the same sampling inlets as the NUIST site. The main aim of the
98 summer campaign was to understand the effects of regional emission control measures during the
99 2014 Young Olympic Games (August 1-September 15) on air quality. Because the two sites locate
100 within the same urban air shed, the measurement provided an opportunity to study seasonal variation
101 of nucleation and its relationship with meteorological variables and gaseous precursors.

102 Sub-3 nm clusters/particles (hereafter referred as particles) were measured with a nano
103 condensation nucleus counter system (nCNC) consisting of a Particle Size Magnifier (PSM model

104 A10, Airmodus Oy, Finland) and a butanol Condensation Particle Counter (model A20, Airmodus
105 Oy, Finland). During the measurement, an ambient air flow of 14 standard liters per minute (slpm)
106 was drawn into building room or trailer via a 72 cm long and 1.0 cm I.D diameter stainless steel (SS)
107 tube, which was extended outside the room/trailer horizontally. PSM then sampled a split flow of 2.5
108 slpm via a SS T-union. The design of the inlet tubing (length and air flow rate) was to minimize the
109 transport loss of nano particles. The size dependent transport survival ratios of sub-3 nm particles in
110 the inlet tubing was estimated (67 %-86 % for 1.4-3.0 nm) and corrected using a particle loss
111 calculator tool (von der Weiden et al., 2009).

112 PSM was operated in a continuous scanning mode with a cycle of 240 steps between saturator
113 flow rates of 0.1 and 1.0 slpm within 240 seconds. The particle cut-off sizes of the nCNC varied with
114 saturation ratios in the saturator (Vanhanen et al., 2011). A step-wise method was used to invert raw
115 scanning data to size spectrum (time resolution: 4 minutes) of sub-3 nm particles, which were
116 classified evenly into 6 size bins, i.e. 1.4-1.6, 1.6-1.9, 1.9-2.2, 2.2-2.4, 2.4-2.7, and 2.7-3.0 nm. The
117 particle number concentrations were then smoothed with a moving average filter for minimizing the
118 effect of noises and fluctuations. The inverted particle number concentrations in the 6 bins were
119 referred as $N_{1.5}$, $N_{1.8}$, $N_{2.0}$, $N_{2.3}$, $N_{2.6}$ and $N_{2.8}$, using mean values of upper and lower size boundaries
120 in each bin. The step-wise method was described in detail by Lehtipalo et al. (2014).

121 Particle size distributions in the range from 3 - 750 nm were obtained by integrating two
122 scanning mobility particle spectrometers (SMPS) with a nano-SMPS (a TSI differential mobility
123 analyzer DMA3085 and a condensation particle counter CPC3776; scanning range: 3 - 64 nm) and a
124 long-SMPS (TSI DMA3081 and CPC3775; scanning range: 64 - 750 nm). During the summer

125 campaign, only the long-SMPS was operated to scan particles from 8 - 350 nm. Scanning cycles of
126 both SMPS systems were 4 minutes, in order to synchronize with the nCNC. The SMPSs sampled
127 ambient air from a separate sampling inlet. The inlet was a 129 cm long and 1.0 cm I.D
128 horizontally-oriented SS tube with an air flow of 14 slpm. The transport loss of particles in the SMPS
129 inlets was corrected using size dependent survival ratios of 85-100% for particles > 3 nm.

130 Sulfur dioxide (SO₂), ozone (O₃), carbon monoxide (CO) and nitrogen oxides (NO and NO₂)
131 concentrations were measured every 1 minute with Thermo Environmental Instruments (model
132 43i-TLE, 49i, 48i, and 42i, respectively). When gaseous SO₂, O₃, NO₂ and CO data were not
133 available, hourly SO₂, O₃, NO₂ and CO were obtained from nearby local Environmental Protection
134 Agency (EPA) monitoring station. PM_{2.5} was monitored with Thermo Scientific TEOM 1405.
135 Meteorological variables including wind speed, wind direction, relative humidity (RH), temperature
136 and solar radiation flux were recorded every 1 hour during the measurement periods. Mean
137 concentrations of PM_{2.5}, SO₂, and O₃ were 79 μ g m⁻³, 10 ppbv and 48 ppbv, respective, during the
138 whole measurement period. Therefore, we regard our measurement environment as a polluted urban
139 atmosphere.

140

141 **2.2 Nucleation event and growth patterns**

142 A criterion was set to determine whether the nCNC detected sub-3nm particles in the atmosphere.
143 The criterion was that total particle concentration reading followed the supersaturation scanning
144 cycle of PSM so that the highest concentrations were measured at lowest cut-off sizes (see also
145 Figure 2 in Lehtipalo et al., 2014). However, it was possible in the step-wise inversion method that

146 the number concentration fluctuation of > 3 nm particles within a 4-min scanning cycle was wrongly
147 inverted to sub-3 nm particles even when sub-3 nm particles actually did not exist according to the
148 above criterion. As a result, the step-wise inversion method always reported a background sub-3 nm
149 particle concentration (N_{sub-3} , i.e. the sum of $N_{1.5}$, $N_{1.8}$, $N_{2.0}$, $N_{2.3}$, $N_{2.6}$ and $N_{2.8}$) of $0.5 \times 10^3 - 2 \times 10^3$
150 cm^{-3} in the nighttime and $3 \times 10^3 - 8 \times 10^3 \text{ cm}^{-3}$ in the daytime. Similar background levels of sub-3 nm
151 particles during non-NPF periods were also reported by other studies that used the nCNC (Kulmala
152 et al., 2013; Lehtipalo et al., 2014; Xiao et al., 2015). Following their procedures, we did not attempt
153 to subtract this background from N_{sub-3} reported in this study.

154 We defined sub-3 nm particle event as sub-3 nm particle occurrence with N_{sub-3} higher than
155 background level persisting for longer than 1 h in the atmosphere. In this study, we used sub-3 nm
156 particle event as an approximate measure of nucleation event. This is because (1) there was an
157 approximately positive linear correlation between N_{sub-3} and nucleation rate ($J_{1.4}$ in this study, see
158 next section) with R^2 of 0.94 (Figure 2), and (2) N_{sub-3} calculation needs only nCNC scanning data
159 and was thus more readily available than $J_{1.4}$ calculation which needs both nCNC and SMPS
160 scanning data. Similar definition has been discussed in our previous studies (Yu et al., 2014a, b).
161 Apparently, a sub-3 nm particle event did not necessarily lead to an NPF event always, but it
162 indicated the intensity and frequency of nucleation in the atmosphere. One focus in this work was to
163 investigate the characteristics of sub-3 nm particle event.

164 Particle growth after nucleation is crucial to determine if nucleated particles could grow to
165 CCN-active sizes. We identified two growth patterns according to size spectrum characteristics in
166 sub-3 nm size range (Figure 3). In a Type A event (Figure 3a or b), size distribution $n(D_p, t)$ was

167 higher at smaller sizes (e.g., 1.4–1.6 nm) than $n(D_p, t)$ at larger sizes (e.g., 2.7–3.0 nm). The size
168 spectrum below 3 nm thus looked like a “volcano”. In a Type B event (Figure 3c or d), $n(D_p, t)$ was
169 lower at smaller sizes than $n(D_p, t)$ at larger sizes (“up-side-down volcano”). For the size range > 3
170 nm, depending on whether a banana-shape growth was seen, we further defined Type A1/A2 and
171 Type B1/B2 events: particles eventually grew to CCN-active sizes in Type A1 and B1 events, while
172 in Type A2 and B2 events banana-shape particle growth to CCN-active sizes was not seen. Therefore,
173 Type A1 and B1 events were equivalent to conventional NPF events based on either DMPS or SMPS
174 measurements.

175 Type B size distribution was more unusual since $n(D_p, t)$ of small particles were less than $n(D_p, t)$
176 of large particles in the sub-3 nm size range. We excluded the possibility of deteriorated nCNC
177 detection efficiencies for small particles due to high particle loading in the sample air. This is
178 because total number concentrations of nCNC during our measurements never approached nCNC
179 upper concentration limit $4 \times 10^5 \text{ cm}^{-3}$, especially in the early stage of nucleation when total particle
180 concentration was rather low. Our nCNC was also calibrated periodically using $\text{H}_2\text{SO}_4\text{-H}_2\text{O}$ particles
181 in a laboratory flow tube to ensure the detection efficiency of the nCNC. The different chemical
182 composition of atmospheric particles could be another factor of lower detection efficiencies. It is
183 well known that organic substances activate less readily in diethylene glycol (e.g. Kangasluoma et al.
184 2014). However, it is accepted in general that larger particles have higher mass fraction of organics
185 than smaller particles in a NPF process. If organic substances activate less readily in DEG, it should
186 be even more difficult to activate larger particles than smaller particles. Therefore, the increasing

187 $n(D_p)$ with D_p (i.e. upside down volcano) could not be simply due to lower detection efficiency of
188 organic substances.

189 **2.3 Formation rate and growth rate calculations with a simplified GDE method**

190 Conventional appearance time method determined growth rates (hereafter, GR) during the initial
191 period of NPF by finding the time steps when newly-formed particles appeared at certain size bins
192 and calculating the GR from the time differences between successive size bins (Kulmala et al., 2012;
193 Lehtipalo et al., 2014). This method was often not applicable to the NPF event with high GR below 3
194 nm, e.g., 0.3 nm/4 min (i.e. 4.5 nm h⁻¹) with size intervals 0.3 nm and scanning time intervals 4
195 minutes in our measurements. Furthermore, sub-3 nm particles were often generated persistently
196 throughout the daytime period. Maximum concentrations in the sub-3 nm size bins could appear
197 around noontime, which is a few hours later than the onset of nucleation. Therefore, we were not
198 able to pinpoint correctly maximum or 50% maximum concentrations at the onset of nucleation.

199 The rapid growth of small particles in the urban atmosphere was the motivation that we used an
200 alternative method to calculate growth rate and formation rate. Here, we analyzed 8 events (listed in
201 Table 1, including both Type A1/A2 and B1/B2 events) in detail, for which complete size spectra
202 from 1.4 - 750 nm were available without distorted, broken or noisy data. Total 8 size bins were
203 classified: 6 evenly-divided size bins in sub-3 nm and 2 size bins in 3-30 nm (3-10 and 10-30 nm).
204 For an aerosol population that is growing through simultaneous condensation and coagulation,
205 aerosol general dynamic equation (GDE) describes the evolution of number concentration in a size
206 bin between particle diameters D_{p1} and D_{p2} ($D_{p2} > D_{p1}$) as:

207
$$\frac{dN(D_{p1}, D_{p2}, t)}{dt} = J(D_{p1}, t) - J(D_{p2}, t) - \text{CoagSnk}(D_{p1}, D_{p2}, t) + \text{CoagSrc}(D_{p1}, D_{p2}, t) \quad (1)$$

208

209 where $N(D_{p1}, D_{p2}, t)$ is the number concentration from D_{p1} to D_{p2} , inverted from nCNC or SMPS
 210 scanning data. J is condensational growth flux (i.e. particle formation rate) across the lower (D_{p1}) or
 211 upper (D_{p2}) boundaries of a size bin. In the first size bin of 1.4-1.6 nm, $J(1.4 \text{ nm}, t)$, or simply $J_{1.4}$,
 212 is the unknown formation rate of the smallest particles that we measured.

213 $\text{CoagSnk}(D_{p1}, D_{p2}, t)$ and $\text{CoagSrc}(D_{p1}, D_{p2}, t)$ are the sink and source terms defining the
 214 coagulation out of and into the size bin between D_{p1} and D_{p2} . Assuming bin k has lower boundary
 215 $D_{p,k}$ and upper boundary $D_{p,k+1}$,

216
$$\text{CoagSnk}(D_{p1}, D_{p2}, t) = N(k, t) \sum_{i=1}^{98} (1 - \theta_{k,i,k}) K_{k,i} N(i, t) \quad (2)$$

217
$$\text{CoagSrc}(D_{p1}, D_{p2}, t) = \frac{1}{2} \sum_{i=1}^{k-1} \sum_{j=1}^{k-1} \theta_{i,j,k} K_{i,j} N(j, t) N(i, t) \quad (3)$$

218 Here $N(i, t)$ is number concentration of bin i . $K_{i,j}$ is coagulation kernel for a collision between
 219 particles from bins i and j . Probability coefficient $\theta_{i,j,k} = 1$, if the volume sum of two coagulating
 220 particles ($v_i + v_j$, here the volume is calculated from the center diameter of a bin) is within the
 221 volume boundaries of bin k . otherwise $\theta_{i,j,k} = 0$. The particle coagulation of total 98 bins was
 222 considered, but the coagulation terms were only needed to be calculated for the smallest 8 bins from
 223 1.4 to 30 nm. According to our calculation, $\text{CoagSrc}(D_{p1}, D_{p2}, t)$ accounted for only 0 - 0.8 % of the
 224 total particle flux into a bin (i.e. $\text{CoagSrc}(D_{p1}, D_{p2}, t) + J(D_{p1}, t)$) in the sub-3 nm size range. This
 225 implied that self coagulation played a negligible role and most of the production flux into a bin is due
 226 to condensational growth from gas molecules.

227 The GDE here is the same as the Eq. 1 by Kuang et al. (2012). In their method, gaseous H_2SO_4
228 was measured simultaneously and a constant $GR(D_p, t) / GR_{\text{H}_2\text{SO}_4}(D_p, t)$ ratio at a given size over time
229 was assumed. Their $GR(D_p, t)$ was then solved by fitting the GDE to the measured size distributions.
230 In our study, however, we did not measure gaseous H_2SO_4 . Instead, $J(30 \text{ nm}, t)$ in the largest size
231 bin, which is the condensational growth flux out of 30 nm, was set to zero. This simplification was
232 valid in the four Type A2/B2 events when particles never grew to $> 30 \text{ nm}$ (March 4, February 19,
233 May 20 and May 16). In the rest four Type A1/B1 events (February 18, December 27, May 15, and
234 August 15), this was also valid during the early NPF period when particles did not grow out of 30 nm
235 and during the late NPF period when particles grew out of 30 nm completely. During the middle
236 period of events (usually around 11:00 AM-14:00 PM), $J(30 \text{ nm}, t)$ was underestimated and thus
237 $J_{1.4}$ could be regarded as a lower estimate. In the four Type A2/B2 events, our calculation showed
238 that J_{10} was only 0-4% of $J_{1.4}$. Xiao et al. (2015) and Kulmala et al. (2013) measured both $J_{1.5}$ and J_3
239 using appearance time method. Their J_3 was less than 7% of $J_{1.5}$. Furthermore, $J_{30}/J_{1.4}$ ratio should be
240 even smaller than $J_{10}/J_{1.4}$ or $J_3/J_{1.5}$ ratios, considering the 8 events were carefully selected to ensure
241 all sub-30 nm particles were grown from nucleation (not emitted directly from emission sources like
242 vehicular engine). All these evidences supported that even if J_{30} was set to 0, $J_{1.4}$ would not be
243 underestimated more than 7% when particles grew cross 30 nm on February 18, December 27, May
244 15, and August 15.

245 Equation 1 requires the balance of condensational growth (J), coagulation terms (CoagSnk and
246 CoagSrc) and the changing rate of particle number concentration (dN/dt). Using Eq. (1) we can
247 therefore calculate the nucleation rate $J(1.4 \text{ nm}, t)$ and formation rates $J(D_p, t)$ across all size bin

248 boundaries from 1.6 to 10 nm. After the formation rates $J(D_p, t)$ were obtained, $GR(D_p, t)$ was
249 calculated from $J(D_p, t)/n(D_p, t)$, where $n(D_p, t)$ is size distribution calculated as $n(D_p, t) = \frac{dN(t)}{dD_p}$
250 for each size bin. On the other hand, the appearance time method could still be applied to (1) the size
251 range of > 3 nm where size intervals were large (2-6 nm), and (2) the size range of < 3 nm when GR
252 was small. The results from appearance time method will also be showed in the next section.

253

254 **3. Results and discussion**

255 Section 3.1, sections 3.2-3.4, section 3.5 and section 3.6 were organized, respectively, to address
256 the following 4 issues: (1) seasonal variation, diurnal variation and limiting factors of nucleation
257 event (represented by sub-3 nm particle event) in the polluted urban atmosphere, (2) time- and size
258 dependent nucleation rate and growth rate of sub-3 nm particles, and their implications for nucleation
259 and growth mechanisms, (3) Inhibited particle growth to CCN-active sizes in strong nucleation
260 events of Type B2, (4) the comparison with other two studies involving sub-3 nm particle
261 measurements in the YRD mega-cities.

262 **3.1 Seasonal and diurnal variations of nucleation event**

263 As seen from Figure 2, there was an approximate linear correlation between N_{sub-3} and $J_{1.4}$ with
264 the slope of $N_{sub-3}/J_{1.4}$ equal to ~ 160 . This seemed to suggest that the average residence time of
265 new particles in the sub-3 nm size range was 160 seconds before they were scavenged due to
266 coagulation or grew out of 3 nm. The sub-3 nm particles observed at the present work were thus

267 formed in situ in the urban atmosphere and not likely to be carried-over by air transport. In this
268 section we used sub-3 nm particle event as an approximate measure of nucleation.

269 We observed significant seasonal characteristics of nucleation event (Figure 4). Nucleation was
270 rare and weak in summer, while it was commonly observed in all other seasons. During our
271 measurements from 2014 to 2015, nucleation events occurred on 81% of all spring observation days
272 (May 2014), 53% in early summer (June 2014), 10% in summer (August and September 2014), and
273 64% in winter (December 2014, February and March 2015). We compared intensity (N_{sub-3}) and
274 frequency of nucleation events, as well as meteorological variables (temperature, RH, wind speed,
275 and solar radiation flux) and gaseous pollutants (SO_2 , NO_2 , CO and O_3) for spring, summer and
276 winter seasons. June was not shown in Figure 4 for comparison, because it was a transit season from
277 spring (May) to summer (August and September). The data were first averaged over the entire event
278 period for each event; and we then used event-averaged data to create box and whistler plots for the 3
279 seasons. $PM_{2.5}$ was used here as a surrogate of condensational sink (CS), because of the more ready
280 availability of $PM_{2.5}$ data than SMPS data.

281 As shown in Figure 4, nucleation in summer was characterized by lowest frequency, lowest
282 N_{sub-3} ($2.2 \times 10^4 \text{ cm}^{-3}$), and short nucleation period (only 1-2 hours). Strict emission control measures
283 during the 2014 Youth Olympic Games resulted in relatively low $PM_{2.5}$ level ($32 \pm 8 \mu \text{g m}^{-3}$),
284 which should favor nucleation. However, relatively low SO_2 concentration ($1.4 \pm 0.6 \text{ ppbv}$), high
285 temperature ($26 \pm 2 \text{ }^\circ\text{C}$), and high RH ($74.3 \pm 4.2 \%$) might not be in favor of nucleation. A simple
286 H_2SO_4 proxy ($\text{Radiation} \times SO_2 / PM_{2.5}$) indicated that summer H_2SO_4 concentration was likely to be the
287 lowest among the 3 seasons, which could explain low nucleation intensity/frequency.

288 We further examined diurnal variations of N_{sub-3} and other variables on event and non-event days
289 in winter (Figure 5). Because nucleation in winter was characterized by Type B event
290 (“up-side-down volcano” below 3 nm), event days were further divided to Type B1 and Type B2
291 events depending on whether banana-shape particle growth was seen. The difference between Type
292 B1 and B2 will be discussed later in Section 3.5. During the non-event days, N_{sub-3} ranged from
293 $2.4 \times 10^3 \text{ cm}^{-3}$ in the night to 8.0×10^3 in the day, which was close to background levels. During the
294 event days, N_{sub-3} in the night was close to that of non-event days, but could reach $8 \times 10^4 - 20 \times 10^4$
295 cm^{-3} in the middle of the day. This was more than 10 times higher than those on the non-event days.
296 From Figure 5 we can see that non-event day had higher concentrations of anthropogenic precursors
297 (indicated by SO_2 , NO_2 , and CO), but nucleation seemed to be limited by higher pre-existing particle
298 surface area (indicated by $\text{PM}_{2.5}$), higher temperature and RH, and lower radiation flux.
299 Photochemistry indicators O_3 was also lower during non-event days.

300 Nucleation in spring was characterized by highest frequency (81%) among all seasons. Highest
301 gaseous pollutant concentration of (H_2SO_4 proxy, SO_2 , NO_2 , CO and O_3) and radiation seemed to the
302 favorable factors to explain this. However, N_{sub-3} in spring ($3.3 \times 10^4 \text{ cm}^{-3}$) was much lower than that
303 in winter ($11.2 \times 10^4 \text{ cm}^{-3}$). Unfavorable factors included high pre-existing particle surface area ($\text{PM}_{2.5}$:
304 $112 \pm 68 \mu \text{g m}^{-3}$) and high temperature ($27 \pm 4 \text{ }^\circ\text{C}$) in spring. Integrating the above seasonal and
305 diurnal variation information in Figure 4 and Figure 5, we tentatively identified that the limiting
306 factors for nucleation in our urban atmosphere were (1) radiation, temperature, RH and CS in winter
307 and spring, and (2) temperature, RH and available gaseous precursors in summer.

308 Out of total 90 measurement days, March 4, 2015 in winter was the only day that we observed
309 significant nocturnal nucleation. Sunrise and sunset were at 6:29 AM and 18:00 PM local time on
310 March 4, but nucleation were observed persistently from 4:00 AM - 20:00 PM. N_{sub-3} increased from
311 $3.5 \times 10^3 \text{ cm}^{-3}$ at 4:00 AM to $6.3 \times 10^4 \text{ cm}^{-3}$ before sunrise. During 10:00-11:00 AM, peak N_{sub-3}
312 reached $3 \times 10^4 \text{ cm}^{-3}$, 3 times higher than the average of all other event days in winter. Apparently,
313 nocturnal nucleation on March 4 could not be explained as carry-over of daytime particles nor being
314 associated with photochemistry. This implied the existence of certain dark nucleation source. There
315 are a number of observations that have also shown nighttime particle formation events in various
316 atmospheric conditions (Junninen et al., 2008; Lehtipalo et al., 2011; Lee et al., 2008; Ortega et al.,
317 2009, 2012; Russell et al., 2007; Suni et al., 2008; Svenningsson et al., 2008; Yu et al., 2014), but the
318 mechanisms behind the nocturnal nucleation are yet still highly speculative. With our instrument
319 capability in this work, we could not deduce any valuable information on the nocturnal nucleation
320 mechanism, except that we found the air mass on 04 March was relatively clean (both CS and gases,
321 mean CS: 0.15 s^{-1}), and temperature and RH (mean: 4.4°C and 33%) were favorable for nucleation.

322

323 **3.2 Size- and time dependent formation rates of sub-3 nm particles**

324 We observed 23 Type A events and 9 Type B events during the measurements. The different
325 size distribution patterns (Figure 3) were probably linked to the mechanism or intensity of nucleation
326 and growth. To address this issue, we first compared the formation rates and growth rates in two
327 types of events. Formation rates J of 1.4, 1.6, 1.9, 2.2, 2.4, 2.7 and 3.0 nm particles were shown in
328 Figure 6 (upper panels) for typical Type A and Type B events. It is obvious that $J_{1.4}$ was much higher

329 on February 18 (Type B) than that on May 15 (Type A). A clear time dependence of J was observed.
330 For example, $J_{1.4}$ was $60 \text{ cm}^{-3} \text{ s}^{-1}$ at the onset of the nucleation event on May 15 and increased to 300
331 $\text{cm}^{-3} \text{ s}^{-1}$ in the middle of the day. In the type B event on February 19, the initial and peak $J_{1.4}$ were
332 2.1×10^2 and $1.2 \times 10^3 \text{ cm}^{-3} \text{ s}^{-1}$ respectively. Therefore, our method provided more information of
333 nucleation than conventional calculation methods that usually showed only an averaged J at the onset
334 of a nucleation event. Our method was also different from Kulmala et al. (2013). Their
335 time-dependent formation rate on an event day was equal to size distribution $n(D_p, t)$ times a constant
336 growth rate at the onset of the event obtained with the appearance time method.

337 The diurnal variation of J implied that nucleation was probably linked to sunlight induced
338 photochemistry. We calculated the correlations between $J_{1.4}$ and an H_2SO_4 proxy for the 8 events of
339 our interest. The H_2SO_4 proxy was calculated following $[\text{H}_2\text{SO}_4] = 8.21 \times 10^{-3} k \cdot \text{Radiation} \cdot$
340 $[\text{SO}_2]^{0.62} \cdot (\text{CS} \cdot \text{RH})^{-0.13}$ (Eq. 8 of Mikkonen et al. 2011), where k is the temperature-dependent
341 reaction-rate constant. Figure 7a show that good linear correlation was usually seen for every single
342 event with R^2 ranging from 0.72 to 0.86 for 6 out of 8 events. A moderate R^2 of 0.56 was obtained
343 for August 15. R^2 was lowest (0.34) on March 4, 2015. This is not surprising because we know
344 March 4 was the only day with nocturnal nucleation during the measurement period. The H_2SO_4
345 proxy was also calculated using the derivation of Petäjä et al. (2009), which resulted in lower R^2 of
346 $\log J_{1.4}$ vs. $\log [\text{H}_2\text{SO}_4]$ for all 8 events. Therefore, in this study we used Mikkonen H_2SO_4 proxy, as
347 it was derived with more comprehensive datasets than Petäjä et al. (2009). The slopes of $\log J_{1.4}$ vs.
348 $\log [\text{H}_2\text{SO}_4]$ were close to 1 in all events (0.82-1.17, excluding March 4), indicating activation theory
349 can explain the nucleation mechanism in our urban atmosphere.

350 If data points of all the 8 events were put together, the linear correlation between H₂SO₄ proxy
351 and $J_{1,4}$ deteriorated (slope=1.1, $R^2=0.17$, Figure 7b). In spite of considerable scattering, most of data
352 points located between $J_{1,4}=10^{-4.1} \times [\text{H}_2\text{SO}_4]$ and $J_{1,4}=10^{-6.3} \times [\text{H}_2\text{SO}_4]$. An interesting finding was
353 that the scattering of $J_{1,4}$ vs. [H₂SO₄] proxy among all 8 events was probably due to temperature or
354 season change (Figure 7b). More specifically, with the same level of H₂SO₄ proxy, $J_{1,4}$ was higher in
355 winter with lower temperature than in spring/summer with higher temperature. There were two
356 possibilities behind the deteriorated linear correlation between H₂SO₄ proxy and $J_{1,4}$: (1) inaccurate
357 H₂SO₄ proxy and (2) other varying factors in nucleation mechanism. First, it was very likely that
358 H₂SO₄ concentrations in our polluted urban atmosphere were overestimated by the H₂SO₄ proxy of
359 Mikkonen et al. (2011), which was based on statistic regression of historical datasets from relatively
360 clean Europe/USA atmosphere. The extent of overestimation may vary with the levels of predictor
361 variables (e.g., SO₂, temperature, CS). Mean SO₂ mixing ratios were 10.5 and 7.3 ppbv in
362 spring/summer and winter during our measurements, respectively. These were 1 order of magnitude
363 higher than SO₂ mixing ratios at the 6 European and USA sites (mean values: 0.23-3.4 ppbv,
364 Mikkonen et al., 2011). Our CS in the 8 events was on the order of magnitude of 10⁻² s⁻¹, again higher
365 than 10⁻³ s⁻¹ in Mikkonen et al. (2011). Mikkonen et al. (2011) had already pointed out that the
366 predictive ability was lower for long term data due to atmospheric condition changes in different
367 seasons.

368 Second, organic condensing vapor concentrations in particle growth events were higher in winter
369 than those in spring/summer (Table 1, see Section 3.4). If the organics were also involved in
370 nucleation, $J_{1,4}$ should be enhanced in winter. The enhancement of nucleation by organics (most

371 likely anthropogenic organics in our urban atmosphere) could be supported by the comparison of $J_{1.4}$
372 dependences on H_2SO_4 between our study and the measurements in the Boreal forest: besides
373 possible H_2SO_4 overestimation, $J_{1.4}=10^{-4.1} \times [\text{H}_2\text{SO}_4] - 10^{-6.3} \times [\text{H}_2\text{SO}_4]$ in our sites was much higher
374 than $J_{1.5}=1.06 \times 10^{-7} [\text{H}_2\text{SO}_4]^{1.1}$ in Hyytiälä during active aerosol formation periods (Kulmala et al.,
375 2013). At last, low temperature itself might enhance nucleation in winter (Brus et al., 2011) via
376 increasing the saturation ratios of all nucleation precursors (e.g., water, H_2SO_4 , organics).

377

378 **3.3 Size- and time dependent growth rates of sub-3 nm particles**

379 Particle size distribution $n(D_p)$ and corresponding $GR(D_p)$ at an instant in time during the events
380 were shown in Figure 6 middle and lower panels. A local minimum of $n(D_p)$ at 2.4 nm, followed by a
381 local maximum somewhere between 2.5 and 10 nm, was seen on May 15, 2014. Such size
382 distribution characteristics on May 15, 2014, as well as on all other Type A event days, was also
383 observed by Kulmala et al. (2013) in the Boreal forest (Figure 1A and S9A in their paper) and by
384 Jiang et al. (2011b) in the urban area of Atlanta, USA (Figure 1 in their paper). We further examined
385 the growth rates in the size range of 1-3 nm on May 15, 2014. It was shown that there was a local
386 maximum of $GR(D_p)$ at 2.4 nm. This could explain why $n(D_p)$ was increasing in 2.4-3 nm size range:
387 when particle condensational flow out of a size bin was slowed down, it was possible that particles
388 flowing into the size bin accumulated, leading to particle number increase in the bin.

389 We saw more unusual behaviors of $n(D_p)$ and $GR(D_p)$ in the Type B event on February 18
390 (Figure 6 right panels): $GR(D_p)$ decreased monotonically in the size range of 1.4 - 3 nm, and

391 accordingly $n(D_p)$ increased monotonically at the same time. A high $GR(D_p)$ of 25 nm h^{-1} was
392 observed at 1.6 nm and $GR(D_p)$ decreased rapidly to 1.7 nm h^{-1} at $\sim 3 \text{ nm}$. If we consider that $GR(D_p)$
393 below 1.6 nm would eventually decrease due to strong Kelvin effect of all possible precursors
394 (H_2SO_4 or organics), the overall trend of $GR(D_p)$ in the Type B event was in fact the same as Type A:
395 for the smallest clusters, growth rate was small (possibly below 1 nm h^{-1}) and increased with D_p . It
396 reached a local maximum somewhere between $1\text{-}3 \text{ nm}$, after which $GR(D_p)$ decreased with D_p . For a
397 typical NPF event, $GR(D_p)$ would eventually increase again after a local minimum between $3\text{-}10 \text{ nm}$.
398 The difference between the Type A event (February 18) and Type B event (May 15) was the D_p of
399 local maximum $GR(D_p)$ (2.4 nm vs. 1.6 nm).

400 The interesting behaviors of $n(D_p)$ and $GR(D_p)$ in our urban atmosphere were different from the
401 stereotyped understanding that steady-state cluster size distribution $n(D_p)$ decreases with D_p in
402 nucleation and GR increases monotonically with D_p in an NPF event. It should be pointed out that if
403 we calculated the overall GR in $1.4\text{-}3 \text{ nm}$, $GR_{1.4-3}$ was 3.6 nm h^{-1} on May 15 and 4.4 nm h^{-1} on
404 February 18, which were still smaller than GR_{3-20} during the initial period of the events (7.7 and 6.0
405 nm h^{-1} , calculated using appearance time method). Table 1 showed that a faster GR_{3-20} than $GR_{1.4-3}$
406 were quite common, except in two events on May 16 and 20 when particles did not grow beyond 3
407 nm . Overall, GR was still increasing with increasing D_p .

408 Kuang et al. (2012) had also reported a local maximum of GR at $\sim 2.6 \text{ nm}$ in an NPF event
409 measured in Atlanta, USA (Figure 1b in their paper). In this study we further point out that GR could
410 decrease monotonically with D_p in $1\text{-}3 \text{ nm}$ range in strong nucleation events. Our GR was calculated
411 from a simplified GDE method, however, the decrease of GR in $1\text{-}3 \text{ nm}$ size range could be easily

412 inferred from the size spectra shown in Figure 3 or Figure 6 middle panels: for a D_{p2} that was larger
413 than D_{p1} , particle formation rate $J(D_{p2})$ must be smaller than $J(D_{p1})$. If we observed a higher $n(D_{p2})$
414 than $n(D_{p1})$, $GR(D_p)$ that was equal to $J(D_p)/n(D_p)$ must be smaller at D_{p2} than D_{p1} .

415

416 **3.4 Growth rate due to condensing organic vapor on newly formed nuclei in sub-3 nm sizes**

417 Apparently, the complicated growth rate behaviours in our polluted urban atmosphere can not be
418 explained by H_2SO_4 condensation alone, not only because H_2SO_4 condensational growth rate
419 ($GR_{H_2SO_4}$, calculated from the H_2SO_4 proxy and shown as black dashed lines in Figure 6) was smaller
420 than the measured growth rate (GR_{meas}), but also because $GR_{H_2SO_4}$ curve should follow a
421 monotonically decreasing trend in > 1 nm sizes assuming a collision-only condensational growth
422 without vaporization (Nieminen et al., 2010).

423 Nano-Köhler theory (Anttila et al., 2004; Kulmala et al., 2004b, c) suggested that when a soluble
424 organic vapor is dissolved in newly formed nuclei of aqueous-phase sulfate at certain size between
425 1-3 nm, the surface organic vapor pressure is lowered and thus assists the growth of the nuclei. Here,
426 we continued our discussion based on the nano-Köhler theory to provide an explanation of GR
427 behaviours observed in our urban atmosphere. We first subtract $GR_{H_2SO_4}$ from GR_{meas} to obtain the
428 growth rate due to a condensing organic vapor (hereafter, denoted as ELVOC, extremely low
429 volatility organic compound):

$$GR_{meas,elvoc} = GR_{meas} - GR_{H_2SO_4}$$

430 where $GR_{H_2SO_4}$ is calculated from the H_2SO_4 proxy concentration $[H_2SO_4]$ following Nieminen et al.
 431 (2010),:

$$432 \quad GR_{H_2SO_4} = \frac{\gamma}{2\rho_{v,H_2SO_4}} \left(1 + \frac{D_{v,H_2SO_4}}{D_p}\right)^2 \left(\frac{8kT}{\pi}\right)^{\frac{1}{2}} \left(\frac{1}{m_p} + \frac{1}{m_{v,H_2SO_4}}\right)^{\frac{1}{2}} m_{v,H_2SO_4} [H_2SO_4] \quad (4)$$

433 and all parameters in Eq.4 are taken from Nieminen et al. (2010) for H_2SO_4 .

434 The size-dependent growth rate due to the uptake of ELVOC was expressed as

$$435 \quad GR_{elvoc} = \frac{\gamma}{2\rho_{v,elvoc}} \left(1 + \frac{D_{v,elvoc}}{D_p}\right)^2 \left(\frac{8kT}{\pi}\right)^{\frac{1}{2}} \left(\frac{1}{m_p} + \frac{1}{m_{v,elvoc}}\right)^{\frac{1}{2}} m_{v,elvoc} (C_{elvoc} - C_{surface}) \quad (5)$$

436 where C_{elvoc} is gas-phase ELVOC concentration far from the particle. The net uptake of
 437 ELVOC is driven by the difference of C_{elvoc} and equilibrium surface concentration over the
 438 particle $C_{surface}$. $C_{surface}$ is determined by the pure component saturation vapor pressure C_{elvoc}^* ,
 439 particle curvature $\exp\left(\frac{4\sigma v}{kTD_p}\right)$ and particle composition:

$$440 \quad C_{surface} = C_{elvoc}^* \exp\left(\frac{4\sigma v}{kTD_p}\right) x_{D_p}$$

441 x_{D_p} is the mole fraction of water-soluble ELVOC in the pseudobinary solution consisting of
 442 ELVOC and the aqueous sulfate nuclei. The pseudobinary solution was treated ideal here. An
 443 example of x_{D_p} as a function of D_p was shown in Figure 8a. Nuclei activation diameter $D_{p,act}$ is the
 444 size that ELVOC fraction begins to increase significantly. For $D_p < D_{p,act}$, x_{D_p} is approximated with
 445 a fixed value (x_0). For $D_p > D_{p,act}$, x_{D_p} increases significantly with the organics being added to the
 446 sulfate core of $D_{p,act}$ size. The size dependent x_{D_p} is approximated as

$$x_{D_p} = \begin{cases} x_0 & , \quad D_p < D_{p,act} \\ x_0 + \frac{(D_p^3 - D_{p,act}^3)/v_{elvoc}}{(D_p^3 - D_{p,act}^3)/v_{elvoc} + D_{p,act}^3/v_{sulfate}} & , \quad D_p \geq D_{p,act} \end{cases}$$

447 Considering strong Kelvin effect, C_{surface} decreases with increasing D_p for $D_p < D_{p,act}$ (Figure
448 8b dashed black line). For $D_p > D_{p,act}$, the rapidly increasing organic fraction in the small size regime
449 of 2-3 nm raises the equilibrium C_{surface} of ELVOC first. Then for 3-6 nm particles that are
450 dominated by organics, C_{surface} decreases to merge with the Kelvin curve of a pure organic droplet
451 (red line, Figure 8b). The complete equilibrium curve of C_{surface} in 1-6 nm (dashed + solid black
452 lines) was shown in Figure 8c. The blue line represented the calculated $C_{\text{elvoc}} - C_{\text{surface}}$. The trend
453 of $C_{\text{elvoc}} - C_{\text{surface}}$ coincided with the size dependence of the measured GR corrected by H_2SO_4
454 ($GR_{\text{meas,elvoc}}$, Figure 8d blue circle). $D_{p,act}$ corresponded to the size with local maximum
455 $GR_{\text{meas,elvoc}}$.

456 We fitted GR_{elvoc} with $GR_{\text{meas,elvoc}}$ in sub-3 nm sizes at an instant in time by adjusting 3 free
457 parameters in Eq. (5): x_0 , C_{elvoc} , and C_{elvoc}^* . Other parameters like surface tension (0.02 N m^{-1}) and
458 molar volume ($135.5 \text{ cm}^3 \text{ mol}^{-1}$) of ELVOC were taken from Kulmala et al. (2004b). Molecule
459 diameter d_v (0.8 nm) and condensed-phase density ρ_v (1.5 g cm^{-3}) of ELVOC were taken from Ehn
460 et al. (2014). Uptake coefficient γ was calculated following Nieminen et al. (2010). The fitting
461 results in Figure 9 showed that the dependence of $GR_{\text{meas,elvoc}}$ on D_p below 3 nm could be well
462 reproduced by Eq. (5) for both Type A and Type B events. Free parameter x_0 determined the
463 magnitude of the dashed black line in Figure 8b. x_0 was fitted to be 0.07-0.42 for the 8 events. C_∞
464 was sensitive to the local maximum $GR_{\text{meas,elvoc}}$ at the $D_{p,act}$. C_{elvoc} , and C_{elvoc}^* determined the
465 local minimum $GR_{\text{meas,elvoc}}$ at the right side of $D_{p,act}$. Therefore, C^* and C_∞ were basically
466 determined by the measured GR (local maximum and local minimum) and not sensitive to x_0 . As
467 shown in Table 1, the condensing organic vapor concentrations C_{elvoc} were $1.7 \times 10^7 - 1.7 \times 10^8 \text{ cm}^{-3}$.

468 The saturation vapor concentration C_{elvoc}^* were 3.3×10^6 - $5.2 \times 10^7 \text{ cm}^{-3}$. They were within the orders
469 of magnitude of 10^7 - 10^8 cm^{-3} and 10^6 - 10^7 cm^{-3} suggested by Kulmala et al. (2004b), respectively.

470 For comparison, the GR calculated from appearance time method was also shown in Figure 9
471 (blue cross) for $> 3 \text{ nm}$ particles on May 15, February 18 and February 19, as well as for sub-3 nm
472 particles on May 20 when particle growth was relatively slow. It can be seen that the GR on May 20
473 calculated from the two methods agreed well with each other, lending credit to our GDE method.
474 The GR in $>10 \text{ nm}$ sizes was usually underestimated by GR_{elvoc} . This could be interpreted as other
475 condensing vapors with higher volatility may contribute to particle growth in the larger particles. It
476 should be noted that the appearance time method followed the time steps when newly-formed
477 particles appeared in successive size bins and thus the GR calculated from appearance time method
478 as not the growth rates at the same instant in time.

479 For all the 8 nucleation events, Table 1 summarizes the measured values of overall growth rate
480 in 1.4-3 nm ($GR_{1.4-3}$), maximum growth rate in 1.4-3 nm ($GR_{\text{max},1.4-3}$), overall growth rate in 3-20 nm
481 (GR_{3-20}), nucleation rate ($J_{1.4}$), activation diameter ($D_{p,act}$), CS , and temperature (T) during the event
482 periods with maximum nucleation rates. Corresponding estimates of Mikkonen H_2SO_4 proxy, C_{elvoc} ,
483 and C_{elvoc}^* were shown in the right 3 columns. It can be seen that in comparison with more
484 conventional Type A events, Type B events usually occurred with (1) higher $J_{1.4}$, $GR_{\text{max},1.4-3}$, $GR_{1.4-3}$,
485 C_{elvoc} , and CS ; (2) smaller $D_{p,act}$; and (3) lower T . However, the H_2SO_4 proxy and GR_{3-20} were
486 similar in Type A and Type B events. Based on these estimations, we concluded that higher ELVOC
487 concentration C_{elvoc} was the key factor leading to the higher $J_{1.4}$ and $GR_{1.4-3}$, which in turn resulted

488 in the different size spectrum pattern in Type B events (“up-side-down volcano”) from in Type A
489 events (“volcano”).

490 It should be noted that the organic vapor concentrations C_{elvoc} in this study were not directly
491 measured, but estimated based on Eq. (4-5). C_{elvoc} , $[\text{H}_2\text{SO}_4]$, mole fraction x_{D_p} and growth rates
492 calculated using Eq. (4-5) were for an instant in time. Aerosol dynamic processes, such as nucleation,
493 coagulation, and the condensation growth of H_2SO_4 and water vapor, were not considered explicitly
494 in Eq. (4-5). In addition, bulk thermodynamics was applied in Eq. (5) for extremely small
495 clusters/particles of sub-3 nm sizes. Therefore, although our calculation provided a possibility to
496 explain the size dependence of growth rate observed in the polluted urban atmosphere, C_{elvoc} in this
497 study was subject to uncertainties in (1) the growth rate derived from the GDE method, (2) the theory
498 by which the growth rate was related to the organic vapor concentration, and (3) H_2SO_4 level which
499 was calculated using Mikkonen et al. (2011) proxy.

500

501 **3.5 Inhibited particle growth to CCN-active sizes in strong nucleation events of Type B2**

502 Type B2 was strong nucleation event that produced rather high concentrations of new particles
503 in sub-20 nm size range (Figure 3d). High concentrations of activating vapor in these events (e.g.,
504 C_{∞} : $1.4\text{-}2.0 \times 10^8 \text{ cm}^{-3}$ on February 18 and March 4) should favor a banana-shape NPF event with fast
505 growth of particles >20 nm, due to weakened Kelvin effect. However, it was puzzling to us why new
506 particles accumulated in 2-20 nm and did not grow further on Type B2 event days (see Figure 3d).
507 We first examined the air mass trajectory characteristics of Type B2 events. Compared with Type B1,

508 Type B2 was characterized by long range transport air masses from far north of China and Mongolia.
509 The lumped trajectories with insignificant wind direction change imply that the air mass in Type B2
510 event was quite uniform. In addition, meteorological and chemical variables (high solar radiation
511 flux and wind speed, low temperature, PM_{2.5}, SO₂, NO₂, CO and O₃, green lines in Figure 5)
512 collectively suggested that Type B2 was typical regional event in homogeneous cold air masses.
513 Therefore, the interrupted growth of new particles was not likely to be a result of wind direction
514 change.

515 As seen from Figure 5, meteorological variables on Type B2 days were generally more favorable
516 in aiding particle growth than on Type B1 days: lower PM_{2.5}, lower temperature, and higher solar
517 radiation flux. The unfavorable factors in Type B2 events, however, included lower concentrations of
518 SO₂, NO₂, and CO (anthropogenic emission indicators), lower secondary photochemical product
519 indicators O₃ and lower particle phase sulfate in 100-1000 nm (X. Ge, private communication, 2015,
520 X. Ge conducted simultaneous AMS measurement during our measurement periods). All these
521 evidences suggested that further particle growth in Type B2 events was limited by certain
522 condensing vapor other than ELVOC. Consequently, although there was a pool of sub-20 nm
523 particles, they were not further “activated” due to the low availability of this condensing vapor.
524 Following the terminology of Donahue et al. (2011, 2012), we called this condensing vapor LVOC
525 (low volatility organic compounds)

526 The above hypothesis was sound if we considered that the identity of LVOC for the growth of
527 particles > 20 nm could be different from ELVOC for sub-3 nm particle growth. Hirsikko et al.
528 (2005) observed that GR_{3-20} demonstrated an opposite seasonal cycle to $GR_{1.3-3}$: GR_{3-20} was higher in

529 summer, whereas $GR_{1.3-3}$ was higher in winter. This suggested that the condensing vapors were
530 different in identity for particles of different sizes. Hirsikko et al. (2005) attributed the condensing
531 vapors for GR_{3-20} to biogenetic VOCs. In our urban atmosphere, according to Figure 5, LVOC was
532 more likely to be from anthropogenic sources associated with SO_2 , NO_x and CO emissions. A picture
533 of the growth process was thus like this: ELVOC of lower volatility, lower concentration and higher
534 water solubility activated inorganic nuclei and accelerated particle growth in smaller sizes. This in
535 turn assisted in the condensation of LVOC of high volatility, low solubility, but with larger amount
536 of mass. The further growth of particles >20 nm, which means significant increment of particle mass,
537 needed continuous supply of LVOC from the anthropogenic sources. On the Type B2 days, LVOC
538 supply was not adequate (low SO_2 , CO and NO_x). As a result, continuous banana-shape particle
539 growth did not take place.

540 **3.6 Comparison with other two sub-3 nm particle studies in the YRD mega-cities**

541 Herrmann et al. (2014), Xiao et al. (2015) and this study investigated sub-3 nm particle
542 occurrences in the polluted mega-cities (Nanjing and Shanghai) of the YRD region. Our study had
543 three advantages over previous studies: (1) we derived time and size-resolved nucleation rate and
544 growth rate, and thus provide more information about NPF, (2) we decoupled the nucleation and
545 growth processes by differentiating sub-3 nm particle event from conventional NPF event. This
546 allowed us to investigate the controlling factors in the 2 processes respectively, (3) our measurement
547 period covered spring, summer and winter seasons, and thus wider ranges of environmental
548 condition variables. Here we compared the results from the three studies. The objective was to

549 investigate how these independent studies contribute collectively to the understanding of NPF in the
550 YRD mega-cities.

551 First, we compared the NPF frequency, nucleation rate, and growth rate. All three studies
552 detected NPF events on about 20% of winter observation days. Including summer and spring with
553 fewer events, we observed the overall NPF frequency was 10% in Nanjing. Using sub-3 nm particle
554 event as an approximate measure of nucleation, we found nucleation frequency actually much higher
555 (47% of all observation days). Xiao et al. (2015) observed that average $J_{1.34}$ at the onset of winter
556 nucleation events was $188 \text{ cm}^{-3}\text{s}^{-1}$ in Shanghai. Using a different GDE method, we found that the
557 event-averaged $J_{1.4}$ ranged from 20 to $500 \text{ cm}^{-3}\text{s}^{-1}$ in the 8 events. Clear diurnal variations of $J_{1.4}$ was
558 observed with peak values up to $2500 \text{ cm}^{-3}\text{s}^{-1}$. In the size range of 3-30 nm, GR was quite close in all
559 three studies, ranging from $4.5\text{-}11 \text{ nm h}^{-1}$. In the sub-3 nm size range, however, our median $GR_{1.4-3}$
560 was 4.3 nm h^{-1} , which was higher than median $GR_{1.35-2.39}$ of 0.94 nm h^{-1} observed in Shanghai.

561 From these comparisons we concluded that (1) nucleation rate in the polluted YRD urban area
562 was clearly higher than those typically observed in most remote or moderately polluted environments
563 (Jiang et al., 2011b; Kuang et al., 2012; Kulmala et al., 2013; Lehtipalo et al., 2009, 2010, 2011; Yu
564 et al., 2014a, b), (2) our results showed a wider range of nucleation rate (a few to $2.5 \times 10^3 \text{ cm}^{-3} \text{ s}^{-1}$)
565 than Xiao et al. (2015) and Herrmann et al. (2014), not only because our data covered 3 seasons, but
566 also because our time-resolved J included the entire nucleation period. (3) GR in the sub-3 nm size
567 range was higher in our study than in Shanghai, partly because the GDE method allowed determining
568 higher GR than appearance time method.

569 Second, we compared the NPF mechanisms in this polluted area reported by the three studies.
570 Based on winter data only, Herrmann et al. (2014) did not find any correlation between
571 temperature and nucleation in Nanjing. But if combining data from different seasons, we found
572 significant negative correlation between $J_{1.4}$ and temperature (Fig 7b), implying atmospheric
573 nucleation was not favoured under high temperature condition. Herrmann et al. (2014) suggested
574 SO_2 was excessive for the winter NPF in Nanjing. We further pointed out that SO_2 may not be
575 excessive in summer and is an unfavourable factor of rare summer nucleation event. Based only on
576 winter observations, Herrmann et al. (2014) and Xiao et al. (2015) identified radiation or H_2SO_4 as
577 the main driving force of NPF and CS as the main obstacle. While we recognized this, we concluded
578 that other environmental variables like temperature and RH can also control the occurrence of
579 atmospheric nucleation under various atmospheric conditions. Furthermore, for the subsequent
580 growth of sub-3 nm particles to CCN-active sizes, the supply of anthropogenic gaseous precursors
581 other than H_2SO_4 can also become a limiting factor.

582 Last, all the three studies tried to correlate Mikkonen et al. (2011)'s H_2SO_4 proxy to nucleation
583 rate or growth rate. Only our study produced a significant correlation between J and $[\text{H}_2\text{SO}_4]^n$
584 ($R^2=0.56-0.86$) with $n=0.82-1.2$ (Fig. 7a). The better correlation was mainly because we used hourly
585 J and $[\text{H}_2\text{SO}_4]$ data, whereas the other 2 studies had fewer data points, i.e., one J value for each event.
586 Xiao et al. (2015) proposed that H_2SO_4 proxy was sufficient to explain their observed $GR_{1.34-3}$. In
587 contrast, our study suggested that other condensing vapors were needed to explain GR in both sub-3
588 nm and >3 nm size ranges.

589

590 4. Conclusion

591 NPF can contribute to CCN only after going through nucleation, initial growth steps and
592 subsequent growth to CCN-active sizes. This study provided the evidences of limiting factors in
593 these processes in a polluted urban atmosphere in China. We observed atmospheric nucleation events
594 on 42 out of total 90 observation days, but particles could grow to CCN-active sizes on only 9 days,
595 which was equivalent to 9 conventional NPF events. In summer, strict emission control measures
596 during the 2014 Youth Olympic Games resulted in relatively low PM_{2.5} and anthropogenic trace
597 gases (SO₂, NO₂, CO and O₃) levels. Infrequent nucleation was thus limited by both low
598 concentrations of gaseous precursors and high temperature and RH in summer. In more polluted
599 winter and spring atmosphere, precursor supply was not limiting anymore; nucleation occurred once
600 meteorological conditions were favorable (i.e. low CS and temperature/RH, higher solar radiation).
601 However, for the further growth of sub-3 nm particles to CCN-active sizes, anthropogenic gaseous
602 precursors again became limiting factors.

603 A simplified GDE method was used in this study to calculate particle formation rates first and
604 then growth rates. Nucleation events were strong in the polluted urban atmosphere of Nanjing. Initial
605 $J_{1.4}$ at the onset and peak $J_{1.4}$ at the noontime could be up to $2.1 \times 10^2 \text{ cm}^{-3} \text{ s}^{-1}$ and $2.5 \times 10^3 \text{ cm}^{-3} \text{ s}^{-1}$,
606 respectively, during the 8 nucleation events selected from different seasons. The diurnal variation of
607 $J_{1.4}$ implied that nucleation was usually linked to sunlight induced photochemistry. Time-dependent
608 $J_{1.4}$ showed good linear correlations with the H₂SO₄ proxy for every single event, except a day with
609 significant nocturnal nucleation. However, the correlation between $J_{1.4}$ and the H₂SO₄ proxy for all 8
610 events deteriorated, which might reflect the effect of temperature or assisting vapor concentration in

611 the nucleation. The deteriorated correlation could also be due to the lower predictive ability of the
612 H₂SO₄ proxy in the polluted urban atmosphere for different seasons.

613 In all nucleation events, a local maximum growth rate was observed between 1-3 nm with *GR* up
614 to 25 nm h⁻¹. This means *GR* was not monotonically increasing with particle size. The overall *GR*_{1.4-3},
615 however, was still smaller than *GR*₃₋₂₀, if particles could grow beyond 3 nm. However, it should be
616 noted that the existence of local maxima *GR* in sub 3 nm is highly sensitive to the uncertainty of size
617 distribution derivation, i.e. the moving average filter was used to smooth original noisy raw data of
618 *N*_{1.5}, *N*_{1.8}, *N*_{2.0}, *N*_{2.3}, *N*_{2.6} and *N*_{2.8}. The noise is due to the nature of sub-3 nm cluster dynamics,
619 environmental conditions and instrumental uncertainties. On the other hand, the *GR* observation is
620 potentially real and might give new insight into cluster dynamics in polluted environments. The local
621 maximum growth rate was interpreted as the solvation effect of organic activating vapor in newly
622 formed inorganic nuclei. Based on our estimation, high ELVOC concentration of 2.3×10⁷ - 2.0×10⁸
623 cm⁻³ was expected to be the key factor leading to high *GR*_{1.4-3}. The varying *GR* of new particle in
624 turn resulted in the different particle growth patterns that we observed in Nanjing.

625

626 Our results call for a more robust proxy of gaseous H₂SO₄ to be developed for polluted urban
627 conditions. The study also highlighted the importance of estimating or measuring activating organic
628 vapor levels (using CI-APi-TOF, for example) in the initial growth steps of atmospheric NPF. Our
629 year-round measurement data provided valuable size evolution data of sub-3 nm clusters/particles to
630 evaluate previous aerosol dynamic models of new particle formation. A robust dynamic model was
631 needed to appropriately treat all aerosol and gas-phase processes in the initial growth steps.

632

633 **Acknowledgements**

634 This work was supported by National Science Foundation of China (grant No. 41405116,
635 21577065 and 91543115), Natural Science Foundation of Jiangsu Province (grant No. BK20140989),
636 Jiangsu Specially Appointed Professor grant and International ST Cooperation Program of China
637 (2014DFA90780). The measurement campaigns were partially funded by the Priority Academic
638 Program Development of Jiangsu Higher Education Institutions (PAPD). J. Zheng acknowledges
639 funding supports from NSFC 41275142 and 41575122. We thank Dr. Vijay P. Kanawade and Dr.
640 Xinlei Ge for valuable discussion. The comments from the editor helped us to improve the
641 manuscript and are highly appreciated by the authors.

642

643 **References:**

644 Almeida, J., Schobesberger, S., Kurten, A., Ortega, I. K., Kupiainen-Maatta, O., Praplan, A. P.,
645 Adamov, A., Amorim, A., Bianchi, F., Breitenlechner, M., David, A., Dommen, J., Donahue, N.
646 M., Downard, A., Dunne, E., Duplissy, J., Ehrhart, S., Flagan, R. C., Franchin, A., Guida, R.,
647 Hakala, J., Hansel, A., Heinritzi, M., Henschel, H., Jokinen, T., Junninen, H., Kajos, M.,
648 Kangasluoma, J., Keskinen, H., Kupc, A., Kurten, T., Kvashin, A. N., Laaksonen, A., Lehtipalo,
649 K., Leiminger, M., Leppa, J., Loukonen, V., Makhmutov, V., Mathot, S., McGrath, M. J.,
650 Nieminen, T., Olenius, T., Onnela, A., Petaja, T., Riccobono, F., Riipinen, I., Rissanen, M.,
651 Rondo, L., Ruuskanen, T., Santos, F. D., Sarnela, N., Schallhart, S., Schnitzhofer, R., Seinfeld, J.

652 H., Simon, M., Sipila, M., Stozhkov, Y., Stratmann, F., Tome, A., Trostl, J., Tsagkogeorgas, G.,
653 Vaattovaara, P., Viisanen, Y., Virtanen, A., Vrtala, A., Wagner, P. E., Weingartner, E., Wex, H.,
654 Williamson, C., Wimmer, D., Ye, P., Yli-Juuti, T., Carslaw, K. S., Kulmala, M., Curtius, J.,
655 Baltensperger, U., Worsnop, D. R., Vehkamäki, H., and Kirkby, J.: Molecular understanding of
656 sulphuric acid-amine particle nucleation in the atmosphere, *Nature*, 502(7471), 359-363,
657 doi:10.1038/nature12663, 2013.

658 Anttila, T., Kerminen, V. M., Kulmala, M., Laaksonen, A., and O'Dowd, C. D.: Modelling the
659 formation of organic particles in the atmosphere, *Atmos. Chem. Phys.*, 4(4), 1071-1083, doi:
660 10.5194/acp-4-1071-2004, 2004.

661 Asmi, E., Sipilä M., Manninen, H. E., Vanhanen, J., Lehtipalo, K., Gagné S., Neitola, K., Mirme,
662 A., Mirme, S., Tamm, E., Uin, J., Komsaare, K., Attoui, M., and Kulmala, M.: Results of the first
663 air ion spectrometer calibration and intercomparison workshop, *Atmos. Chem. Phys.*, 9(1),
664 141-154, doi: 10.5194/acp-9-141-2009, 2009.

665 Brus, D., Neitola, K., Hyvärinen, A.-P., Petäjä T., Vanhanen, J., Sipilä M., Paasonen, P., Kulmala,
666 M., and Lihavainen, H.: Homogenous nucleation of sulfuric acid and water at close to
667 atmospherically relevant conditions, *Atmos. Chem. Phys.*, 11(11), 5277-5287, doi:
668 10.5194/acp-11-5277-2011, 2011.

669 Chan, C. K., and Yao, X.: Air pollution in mega cities in China, *Atmos. Environ.*, 42(1), 1-42,
670 doi: :10.1016/j.atmosenv.2007.09.003.

671 Donahue, N. M., Trump, E. R., Pierce, J. R., and Riipinen, I.: Theoretical constraints on pure
672 vapor-pressure driven condensation of organics to ultrafine particles, *Geophys. Res. Lett.*, 38(16),
673 L16801, doi: 10.1029/2011gl048115, 2011.

674 Donahue, N. M., Kroll, J. H., Pandis, S. N., and Robinson, A. L.: A two-dimensional volatility basis
675 set – Part 2: Diagnostics of organic-aerosol evolution, *Atmos. Chem. Phys.*, 12(2), 615-634, doi:
676 10.5194/acp-12-615-2012, 2012.

677 Ehn, M., Thornton, J. A., Kleist, E., Sipila, M., Junninen, H., Pullinen, I., Springer, M., Rubach, F.,
678 Tillmann, R., Lee, B., Lopez-Hilfiker, F., Andres, S., Acir, I.-H., Rissanen, M., Jokinen, T.,
679 Schobesberger, S., Kangasluoma, J., Kontkanen, J., Nieminen, T., Kurten, T., Nielsen, L. B.,
680 Jorgensen, S., Kjaergaard, H. G., Canagaratna, M., Maso, M. D., Berndt, T., Petaja, T., Wahner,
681 A., Kerminen, V. M., Kulmala, M., Worsnop, D. R., Wildt, J., and Mentel, T. F.: A large source
682 of low-volatility secondary organic aerosol, *Nature*, 506(7489), 476-479, doi:
683 10.1038/nature13032, 2014.

684 Herrmann, E., Ding, A. J., Kerminen, V.-M., Petäjä T., Yang, X. Q., Sun, J. N., Qi, X. M.,
685 Manninen, H., Hakala, J., Nieminen, T., Aalto, P. P., Kulmala, M., and Fu, C. B.: Aerosols and
686 nucleation in eastern China: first insights from the new SORPES-NJU station, *Atmos. Chem.*
687 *Phys.*, 14, 2169-2183, doi: 10.5194/acp-14-2169-2014, 2014.

688 Hirsikko, A., Laakso, L., Horrak, U., Aalto, P. P., Kerminen, V. M., and Kulmala, M.: Annual and
689 size dependent variation of growth rates and ion concentrations in boreal forest, *Boreal Environ.*
690 *Res.*, 10, 357-469, 2005.

691 Jiang, J., Chen, M., Kuang, C., Attoui, M., and McMurry, P. H.: Electrical Mobility Spectrometer
692 Using a Diethylene Glycol Condensation Particle Counter for Measurement of Aerosol Size
693 Distributions Down to 1 nm, *Aerosol Sci. Technol.*, 45(4), 510-521, doi:
694 10.1080/02786826.2010.547538, 2011a.

695 Jiang, J., Zhao, J., Chen, M., Eisele, F. L., Scheckman, J., Williams, B. J., Kuang, C., and McMurry,
696 P. H.: First Measurements of Neutral Atmospheric Cluster and 1-2 nm Particle Number Size
697 Distributions During Nucleation Events, *Aerosol Sci. Technol.*, 45(4), II-V, doi:
698 10.1080/02786826.2010.546817, 2011b.

699 Jokinen, T., Sipilä M., Junninen, H., Ehn, M., Lönn, G., Hakala, J., Petäjä T., Mauldin III, R. L.,
700 Kulmala, M., and Worsnop, D. R.: Atmospheric sulphuric acid and neutral cluster measurements
701 using CI-API-TOF, *Atmos. Chem. Phys.*, 12(9), 4117-4125, doi: 10.5194/acp-12-4117-2012,
702 2012.

703 Junninen, H., Hulkkonen, M., Riipinen, I., Nieminen, T., Hirsikko, A., Suni, T., Boy, M., Lee, S.-H.,
704 Vana, M., Tammet, T., Kerminen, V. M., and Kulmala, M.: Observations on nocturnal growth of
705 atmospheric clusters, *Tellus Ser. B*, 60, 365-371, doi:10.1111/j.1600-0889.2008.00356.x, 2008.

706 Junninen, H., Ehn, M., Petäjä T., Luosujärvi, L., Kotiaho, T., Kostianen, R., Rohner, U., Gonin, M.,
707 Fuhrer, K., Kulmala, M., and Worsnop, D. R.: A high-resolution mass spectrometer to measure
708 atmospheric ion composition, *Atmos. Meas. Tech.*, 3, 1039-1053, doi: 10.5194/amtd-3-599-2010,
709 2010.

710 Kangasluoma, J., Kuang, C., Wimmer, D., Rissanen, M. P., Lehtipalo, K., Ehn, M., Worsnop, D.R.,
711 Wang, J., Kulmala, M. and Petäjä T.: Sub-3 nm particle size and composition dependent
712 response of a nano-CPC battery. *Atmos. Meas. Tech.*, 7, 689-700, doi: 10.5194/amt-7-689-2014,
713 2014.

714 Kirkby, J., Curtius, J., Almeida, J., Dunne, E., Duplissy, J., Ehrhart, S., Franchin, A., Gagne, S.,
715 Ickes, L., Kurten, A., Kupc, A., Metzger, A., Riccobono, F., Rondo, L., Schobesberger, S.,
716 Tsagkogeorgas, G., Wimmer, D., Amorim, A., Bianchi, F., Breitenlechner, M., David, A.,
717 Dommen, J., Downard, A., Ehn, M., Flagan, R. C., Haider, S., Hansel, A., Hauser, D., Jud, W.,
718 Junninen, H., Kreissl, F., Kvashin, A., Laaksonen, A., Lehtipalo, K., Lima, J., Lovejoy, E. R.,
719 Makhmutov, V., Mathot, S., Mikkila, J., Minginette, P., Mogo, S., Nieminen, T., Onnela, A.,
720 Pereira, P., Petaja, T., Schnitzhofer, R., Seinfeld, J. H., Sipila, M., Stozhkov, Y., Stratmann, F.,
721 Tome, A., Vanhanen, J., Viisanen, Y., Vrtala, A., Wagner, P. E., Walther, H., Weingartner, E.,
722 Wex, H., Winkler, P. M., Carslaw, K. S., Worsnop, D. R., Baltensperger, U., and Kulmala, M.:
723 Role of sulphuric acid, ammonia and galactic cosmic rays in atmospheric aerosol nucleation,
724 *Nature*, 476(7361), 429-433, doi:10.1038/nature10343, 2011.

725 Kuang, C., Chen, M., Zhao, J., Smith, J., McMurry, P. H., and Wang, J.: Size- and time-resolved
726 growth rate measurements of 1 to 5 nm freshly formed atmospheric nuclei, *Atmos. Chem. Phys.*,
727 12(9), 3573-3589, doi: 10.5194/acpd-11-25427-2011, 2012.

728 Kulmala, M., Pirjola, L., and Makela, J. M.: Stable sulfate clusters as a source of new atmospheric
729 particles, *Nature*, 404, 60-66, doi: 10.1038/35003550, 2000.

730 Kulmala, M., Laakso, L., Lehtinen, K. E. J., Riipinen, I., Dal Maso, M., Lauria, A., Kerminen, V. M.,
731 Birmili, W., McMurry, P.H.: Formation and growth rates of ultrafine atmosphere particles: A
732 review of observations, *J. Aerosol. Sci.*, 35, 143-176, 2004a.

733 Kulmala, M., Kerminen, V. M., Anntila, T., Laaksonen, A., and O'Dowd, C. D.: Organic aerosol
734 formation via sulfate cluster activation, *J. Geophys. Res.*, 109, D04205, doi:
735 10.1029/2003JD003961, 2004b.

736 Kulmala, M., Laakso, L., Lehtinen, K. E. J., Riipinen, I., Dal Maso, M., Anttila, T., Kerminen, V.-M.,
737 Hõrrak, U., Vana, M., and Tammet, H.: Initial steps of aerosol growth, *Atmos. Chem. Phys.*,
738 4(11), 2553-2560, doi: 10.5194/acp-4-2553-2004, 2004c.

739 Kulmala, M., Petäjä T., Nieminen, T., Sipilä M., Manninen, H. E., Lehtipalo, K., Dal Maso, M.,
740 Aalto, P. P., Junninen, H., Paasonen, P., Riipinen, I., Lehtinen, K. E. J., Laaksonen, A., and
741 Kerminen, V. M.: Measurement of the nucleation of atmospheric aerosol particles, *Nat. Protocols*,
742 7(9), 1651-1667, doi: 10.1038/nprot.2012.091, 2012.

743 Kulmala, M., Kontkanen, J., Junninen, H., Lehtipalo, K., Manninen, H. E., Nieminen, T., Petäjä T.,
744 Sipilä M., Schobesberger, S., Rantala, P., Franchin, A., Jokinen, T., Järvinen, E., Äijälä M.,
745 Kangasluoma, J., Hakala, J., Aalto, P. P., Paasonen, P., Mikkilä J., Vanhanen, J., Aalto, J.,
746 Hakola, H., Makkonen, U., Ruuskanen, T., Mauldin, R. L., Duplissy, J., Vehkamäki, H., Bäck, J.,
747 Kortelainen, A., Riipinen, I., Kurtén, T., Johnston, M. V., Smith, J. N., Ehn, M., Mentel, T. F.,
748 Lehtinen, K. E. J., Laaksonen, A., Kerminen, V. M., and Worsnop, D. R.: Direct Observations of

749 Atmospheric Aerosol Nucleation, *Science*, 339(6122), 943-946, doi: 10.1126/science.1227385,
750 2013.

751 Kulmala, M., Petäjä T., Ehn, M., Thornton, J., Sipilä M., Worsnop, D. R. and Kerminen, V. M.:
752 Chemistry of Atmospheric Nucleation: On the Recent Advances on Precursor Characterization
753 and Atmospheric Cluster Composition in Connection with Atmospheric New Particle Formation,
754 *Annu. Rev. Phys. Chem.*, 65, 21–37, doi: 10.1146/annurev-physchem-040412-110014, 2014.

755 Kürten, A., Jokinen, T., Simon, M., Sipilä M., Sarnela, N., Junninen, H., Adamov, A., Almeida, J.,
756 Amorim, A., Bianchi, F., Breitenlechner, M., Dommen, J., Donahue, N. M., Duplissy, J., Ehrhart,
757 S., Flagan, R. C., Franchin, A., Hakala, J., Hansel, A., Heinritzi, M., Hutterli, M., Kangasluoma,
758 J., Kirkby, J., Laaksonen, A., Lehtipalo, K., Leiminger, M., Makhmutov, V., Mathot, S., Onnela,
759 A., Petäjä T., Praplan, A. P., Riccobono, F., Rissanen, M. P., Rondo, L., Schobesberger, S.,
760 Seinfeld, J. H., Steiner, G., Tomé A., Tröstl, J., Winkler, P. M., Williamson, C., Wimmer, D., Ye,
761 P., Baltensperger, U., Carslaw, K. S., Kulmala, M., Worsnop, D. R., and Curtius, J.: Neutral
762 molecular cluster formation of sulfuric acid–dimethylamine observed in real time under
763 atmospheric conditions, *Proc. Natl. Acad. Sci. U.S.A.*, 111(42), 15019-15024,
764 doi:10.1073/pnas.1404853111, 2014.

765 Lee, S. H., Young, L. H., Benson, D. R., Kulmala, M., Junninen, H., Suni, T., Campos, T., Rogers, D.
766 C., and Jensen, J.: Observations of nighttime new particle formation in the troposphere, *J.*
767 *Geophys. Res.*, 113, D10210, doi: 10.1029/12007JD009351, 2008.

768 Lehtipalo, K., Sipil ä M., Riipinen, I., Nieminen, T., and Kulmala, M.: Analysis of atmospheric
769 neutral and charged molecular clusters in boreal forest using pulse-height CPC, *Atmos. Chem.*
770 *Phys.*, 9, 4177–4184, 2009.

771 Lehtipalo, K., Sipila, M., Junninen, H., Ehn, M., Berndt, T., Kajos, M. K., Worsnop, D. R., Petaja, T.,
772 and Kulmala, M.: Nanoparticles in boreal forest and coastal environment: a comparison of
773 observations and implications of the nucleation mechanism, *Atmos. Chem. Phys.*, 10, 7009-7016,
774 2010.

775 Lehtipalo, K., Sipila, M., Junninen, H., Ehn, M., Berndt, T., Kajos, M. K., Worsnop, D. R., Petaja, T.,
776 and Kulmala, M.: Observations of Nano-CN in the Nocturnal Boreal Forest, *Aerosol Sci.*
777 *Technol.*, 45(4), 499-509, doi: 10.1080/02786826.2010.547537, 2011.

778 Lehtipalo., K., Lepp ä, J., Kontkanen., J., Kangasluoma., J., Franchin., A., Wimmer., D.,
779 Schobesberger., S., Junninen., H., Pet ä ä, T., Sipil ä, M., Mikkil ä, J., Vanhanen., J., Worsnop., D.
780 R., and Kulmala, M.: Methods for determining particle size distribution and growth rates between
781 1 and 3 nm using the Particle Size Magnifier, *Boreal Environ. Res.*, 19, 215–236, 2014.

782 Matsui, H., Koike, M., Takegawa, N., Kondo, Y., Takami, A., Takamura, T., Yoon, S., Kim, S. W.,
783 Lim, H. C., and Fast, J. D.: Spatial and temporal variations of new particle formation in East Asia
784 using an NPF-explicit WRF-chem model: North-south contrast in new particle formation
785 frequency, *J. Geophys. Res.*, 118(20), 11,647-611,663, doi:10.1002/jgrd.50821, 2013.

786 Merikanto, J., Spracklen, D. V., Mann, G. W., Pickering, S. J., and Carslaw, K. S.: Impact of
787 nucleation on global CCN, *Atmos. Chem. Phys.*, doi: 10.5194/acp-9-8601-2009, 9, 8601-8616,
788 2009.

789 Mikkonen, S., Romakkaniemi, S., Smith, J. N., Korhonen, H., Petäjä T., Plass-Duelmer, C., Boy, M.,
790 McMurry, P. H., Lehtinen, K. E. J., Joutsensaari, J., Hamed, A., Mauldin III, R. L., Birmili, W.,
791 Spindler, G., Arnold, F., Kulmala, M., and Laaksonen, A.: A statistical proxy for sulphuric acid
792 concentration, *Atmos. Chem. Phys.*, 11:11319-11334, doi: 10.5194/acpd-11-20141-2011, 2011.

793 Nieminen, T., Lehtinen, K. E. J., and Kulmala, M.: Sub-10 nm particle growth by vapor
794 condensation - effects of vapor molecule size and particle thermal speed, *Atmos. Chem. Phys.*,
795 10(20), 9773-9779, doi: 10.5194/acp-10-9773-2010, 2010.

796 Ortega, I. K., Suni, T., Gronholm, T., Boy, M., Hakola, H., Hellen, H., Valmari, T., Arvela, H.,
797 Vehkamäki, H., and Kulmala, M.: Is eucalyptol the cause of nocturnal events observed in
798 Australia?, *Boreal Environ. Res.*, 14(4), 606-615, 2009.

799 Ortega, I. K., Suni, T., Boy, M., Grönholm, T., Manninen, H. E., Nieminen, T., Ehn, M., Junninen,
800 H., Hakola, H., Hellén, H., Valmari, T., Arvela, H., Zegelin, S., Hughes, D., Kitchen, M., Cleugh,
801 H., Worsnop, D. R., Kulmala, M., and Kerminen, V. M.: New insights into nocturnal nucleation,
802 *Atmos. Chem. Phys.*, 12(9), 4297-4312, doi:10.5194/acp-12-4297-2012, 2012.

803 Petäjä T., Mauldin, III, R. L., Kosciuch, E., McGrath, J., Nieminen, T., Paasonen, P., Boy, M.,
804 Adamov, A., Kotiaho, T., and Kulmala, M.: Sulfuric acid and OH concentrations in a boreal
805 forest site, *Atmos. Chem. Phys.*, 9, 7435–7448, doi:10.5194/acp-9-7435-2009, 2009.

806 Pierce, J. R., and Adams, P. J.: Uncertainty in global CCN concentrations from uncertain aerosol
807 nucleation and primary emission rates, *Atmos. Chem. Phys.*, 9(4), 1339-1356, doi:
808 10.5194/acp-9-1339-2009, 2009.

809 Riccobono, F., Schobesberger, S., Scott, C. E., Dommen, J., Ortega, I. K., Rondo, L., Almeida, J.,
810 Amorim, A., Bianchi, F., Breitenlechner, M., David, A., Downard, A., Dunne, E. M., Duplissy, J.,
811 Ehrhart, S., Flagan, R. C., Franchin, A., Hansel, A., Junninen, H., Kajos, M., Keskinen, H., Kupc,
812 A., Kürten, A., Kvashin, A. N., Laaksonen, A., Lehtipalo, K., Makhmutov, V., Mathot, S.,
813 Nieminen, T., Onnela, A., Petäjä T., Praplan, A. P., Santos, F. D., Schallhart, S., Seinfeld, J. H.,
814 Sipilä M., Spracklen, D. V., Stozhkov, Y., Stratmann, F., Tomé A., Tsagkogeorgas, G.,
815 Vaattovaara, P., Viisanen, Y., Vrtala, A., Wagner, P. E., Weingartner, E., Wex, H., Wimmer, D.,
816 Carslaw, K. S., Curtius, J., Donahue, N. M., Kirkby, J., Kulmala, M., Worsnop, D. R., and
817 Baltensperger, U.: Oxidation Products of Biogenic Emissions Contribute to Nucleation of
818 Atmospheric Particles, *Science*, 344(6185), 717-721, doi:10.1126/science.1243527, 2014.

819 Riipinen, I., Yli-Juuti, T., Pierce, J. R., Petaja, T., Worsnop, D. R., Kulmala, M., and Donahue, N.
820 M.: The contribution of organics to atmospheric nanoparticle growth, *Nature Geosci.*, 5(7),
821 453-458, doi: 10.1038/NGEO1499, 2012.

822 Russell, L. M., Mensah, A. A., Fischer, E. V., Sive, B. C., Varner, R. K., Keene, W. C., Stutz, J., and
823 Pszenny, A. A. P.: Nanoparticle growth following photochemical α - and β -pinene oxidation at
824 Appledore Island during International Consortium for Research on Transport and
825 Transformation/Chemistry of Halogens at the Isles of Shoals 2004, *J. Geophys. Res.*, 112(D10),
826 D10S21, doi:10.1029/2006jd007736, 2007. Seinfeld, J. H., and Pandis, S. N.: Atmospheric

827 chemistry and physics: from air pollution to climate change, 2nd ed., John Wiley and Sons. Inc.,
828 New York, 2006.

829 Schobesberger, S., Junninen, H., Bianchi, F., Lönn, G., Ehn, M., Lehtipalo, K., Dommen, J., Ehrhart,
830 S., Ortega, I. K., Franchin, A., Nieminen, T., Riccobono, F., Hutterli, M., Duplissy, J., Almeida,
831 J., Amorim, A., Breitenlechner, M., Downard, A. J., Dunne, E. M., Flagan, R. C., Kajos, M.,
832 Keskinen, H., Kirkby, J., Kupc, A., Kürten, A., Kurtén, T., Laaksonen, A., Mathot, S., Onnela, A.,
833 Praplan, A. P., Rondo, L., Santos, F. D., Schallhart, S., Schnitzhofer, R., Sipilä M., Tomé A.,
834 Tsagkogeorgas, G., Vehkamäki, H., Wimmer, D., Baltensperger, U., Carslaw, K. S., Curtius, J.,
835 Hansel, A., Petäjä T., Kulmala, M., Donahue, N. M., and Worsnop, D. R.: Molecular
836 understanding of atmospheric particle formation from sulfuric acid and large oxidized organic
837 molecules, *Proc. Natl. Acad. Sci. U.S.A.*, doi:10.1073/pnas.1306973110, 2013.

838 Sipilä, M., Lehtipalo, K., Attoui, M., Neitola, K., Petäjä T., Aalto, P. P., O'Dowd, C. D., and
839 Kulmala, M.: Laboratory Verification of PH-CPC's Ability to Monitor Atmospheric Sub-3 nm
840 Clusters, *Aerosol Sci. Technol.*, 43(2), 126-135, doi: 10.1080/02786820802506227, 2009.

841 Spracklen, D. V., Carslaw, K. S., Kulmala, M., Kerminen, V.-M., Sihto, S.-L., Riipinen, I.,
842 Merikanto, J., Mann, G. W., Chipperfield, M. P., Wiedensohler, A., Birmili, W., and Lihavainen,
843 H.: Contribution of particle formation to global cloud condensation nuclei concentrations,
844 *Geophys. Res. Lett.*, 35(6), L06808, doi:10.1029/2007GL033038, 2008.

845 Suni, T., Kulmala, M., Hirsikko, A., Bergman, T., Laakso, L., Aalto, P. P., Leuning, R., Cleugh, H.,
846 Zegelin, S., Hughes, D., van Gorsel, E., Kitchen, M., Vana, M., Hõrrak, U., Mirme, S., Mirme, A.,

847 Sevanto, S., Twining, J., and Tadros, C.: Formation and characteristics of ions and charged
848 aerosol particles in a native Australian Eucalypt forest, *Atmos. Chem. Phys.*, 8(1), 129-139,
849 doi:10.5194/acp-8-129-2008, 2008.

850 Svenningsson, B., Arneth, A., Hayward, S., Holst, T., Massling, A., Swietlicko, E., Hirsikko, A.,
851 Junninen, H., Riipinen, I., Vana, M., Dal Maso, M., Hussein, T., and Kulmala, M.: Aerosol
852 particle formation events and analysis of high growth rates observed above a subarctic
853 wetland-forest mosaic, *Tellus*, 60(B), 353-365, doi:10.1111/j.1600-0889.2008.00351.x, 2008.

854 Vanhanen, J., Mikkilä, J., Lehtipalo, K., Sipilä, M., Manninen, H. E., Siivola, E., Petaja, T., and
855 Kulmala, M.: Particle Size Magnifier for Nano-CN Detection, *Aerosol Sci. Technol.*, 45(4),
856 533-542, doi: 10.1080/02786826.2010.547889, 2011.

857 von der Weiden, S. L., Drewnick, F., and Borrmann, S.: Particle Loss Calculator – a new software
858 tool for the assessment of the performance of aerosol inlet systems, *Atmos. Meas. Tech.*, 2(2),
859 479-494, doi: 10.5194/amt-2-479-2009, 2009.

860 Wiedensohler, A., Cheng, Y. F., Nowak, A., Wehner, B., Achtert, P., Berghof, M., Birmili, W., Wu,
861 Z. J., Hu, M., Zhu, T., Takegawa, N., Kita, K., Kondo, Y., Lou, S. R., Hofzumahaus, A., Holland,
862 F., Wahner, A., Gunthe, S. S., Rose, D., Su, H., and Pöschl, U.: Rapid aerosol particle growth and
863 increase of cloud condensation nucleus activity by secondary aerosol formation and condensation:
864 A case study for regional air pollution in northeastern China, *J. Geophys. Res.*, 114(D2), D00G08,
865 doi:10.1029/2008jd010884, 2009.

866 Wang, J., and Wexler, A. S.: Adsorption of organic molecules may explain growth of newly
867 nucleated clusters and new particle formation, *Geophys. Res. Lett.*, 11, 2834-2838, doi:
868 10.1002/grl.50455, 2013.

869 Wang, J., McGraw, R. L., and Kuang, C.: Growth of atmospheric nano-particles by heterogeneous
870 nucleation of organic vapor, *Atmos. Chem. Phys.*, 13(13), 6523-6531, doi:
871 10.5194/acp-13-6523-2013, 2013.

872 Xiao, S., Wang, M. Y., Yao, L., Kulmala, M., Zhou, B., Yang, X., Chen, J. M., Wang, D. F., Fu, Q.
873 Y., Worsnop, D. R., and Wang, L.: Strong atmospheric new particle formation in winter in urban
874 Shanghai, China, *Atmos. Chem. Phys.*, 15(4), 1769-1781, doi: 10.5194/acp-15-1769-2015, 2015.

875 Yu, H., Gannet Hallar, A., You, Y., Sedlacek, A., Springston, S., Kanawade, V. P., Lee, Y. N., Wang,
876 J., Kuang, C., McGraw, R. L., McCubbin, I., Mikkilä J., and Lee, S. H.: Sub-3 nm particles
877 observed at the coastal and continental sites in the United States, *J. Geophys. Res.*, 119(2),
878 2013JD020841, doi: 10.1002/2013jd020841, 2014a.

879 Yu, H., Ortega, J., Smith, J. N., Guenther, A. B., Kanawade, V. P., You, Y., Liu, Y., Hosman, K.,
880 Karl, T., Seco, R., Geron, C., Pallardy, S. G., Gu, L., Mikkilä J., and Lee, S. H.: New Particle
881 Formation and Growth in an Isoprene-Dominated Ozark Forest: From Sub-5 nm to CCN-Active
882 Sizes, *Aerosol Sci. Technol.*, 48(12), 1285-1298, doi: 10.1080/02786826.2014.984801, 2014b.

883 Yu, F., and Luo, G.: Simulation of particle size distribution with a global aerosol model: contribution
884 of nucleation to aerosol and CCN number concentrations, *Atmos. Chem. Phys.*, 9(20), 7691-7710,
885 doi:10.5194/acp-9-7691-2009, 2009.

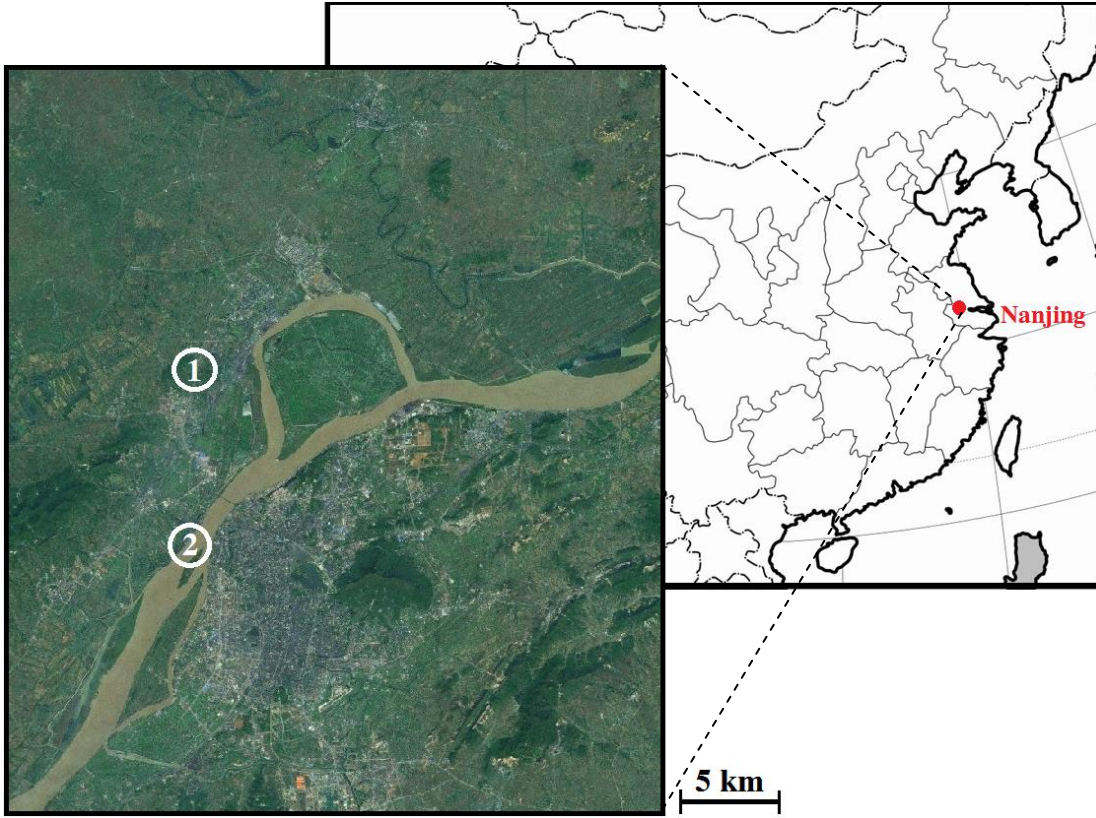
886 Yue, D. L., Hu, M., Zhang, R. Y., Wu, Z. J., Su, H., Wang, Z. B., Peng, J. F., He, L. Y., Huang, X. F.,
887 Gong, Y. G., and Wiedensohler, A.: Potential contribution of new particle formation to cloud
888 condensation nuclei in Beijing, *Atmos. Environ.*, 45(33), 6070-6077,
889 doi:10.1016/j.atmosenv.2011.07.037, 2011.

890 Zhang, K. M., and Wexler, A. S.: A hypothesis for growth of fresh atmospheric nuclei, *J. Geophys.*
891 *Res.*, 107, 4577, doi: 10.1029/2002JD002180, 2002.

892 Zhao, J., Eisele, F. L., Titcombe, M., Kuang, C., and McMurry, P. H.: Chemical ionization mass
893 spectrometric measurements of atmospheric neutral clusters using the cluster-CIMS, *J. Geophys.*
894 *Res.*, 115, D08205, doi: 10.1029/2009JD012606, 2010.

895 Table 1. Activation diameter ($D_{p,act}$), maximum growth rate in 1.4-3 nm ($GR_{max, 1.4-3}$), overall growth rate in 1.4-3 nm ($GR_{1.4-3}$), overall growth
896 rate in 3-20 nm (GR_{3-20}), nucleation rate ($J_{1.4}$), condensation sink (CS), and temperature (T) of selected nucleation events. Estimated gas-phase
897 condensing vapor concentrations C_{elvoc} , pure saturation concentration of condensing vapor over flat surface C_{elvoc}^* , and Mikkonen H_2SO_4 proxy
898 were shown in right 3 columns. All data were for the time periods with maximum nucleation rates.

Type	Date	$D_{p,act}$ (nm)	$GR_{max,1.4-3}$ (nm h ⁻¹)	$GR_{1.4-3}$ (nm h ⁻¹)	GR_{3-20} (nm h ⁻¹)	$J_{1.4}$ (cm ⁻³ s ⁻¹)	T (°C)	CS (10 ⁻² s ⁻¹)	Mikkonen H_2SO_4 proxy (cm ⁻³)	C_{elvoc} (cm ⁻³)	C_{elvoc}^* (cm ⁻³)
A1	May 15, 2014	2.4	6.4	3.6	7.7	3.0×10^2	20.8	1.6	2.9×10^7	3.5×10^7	6.3×10^6
A1	Aug 15, 2014	2.4	14.5	7.1	7.7	2.0×10^2	26.1	1.8	3.1×10^7	8.5×10^7	2.1×10^7
A2	May 16, 2014	2.4	3.8	1.9	0	95	25.3	1.9	1.4×10^7	2.5×10^7	4.6×10^6
A2	May 20, 2014	2.2	2.9	1.6	0	92	24.1	1.9	1.3×10^7	1.7×10^7	3.3×10^6
B1	Feb 18, 2015	1.6	25.9	4.4	6.0	1.1×10^3	8.2	3.3	3.9×10^7	1.4×10^8	3.0×10^7
B1	Dec 27, 2014	1.6	17.7	4.2	5.5	1.9×10^2	7.6	2.8	3.5×10^7	1.1×10^8	2.2×10^7
B2	Feb 19, 2015	1.9	25.0	8.9	10.1	8.0×10^2	7.4	3.2	3.7×10^7	1.7×10^8	5.2×10^7
B2	Mar 4, 2015	1.9	18.0	5.8	8.7	2.5×10^3	3.9	2.2	4.8×10^7	1.3×10^8	1.1×10^7



899

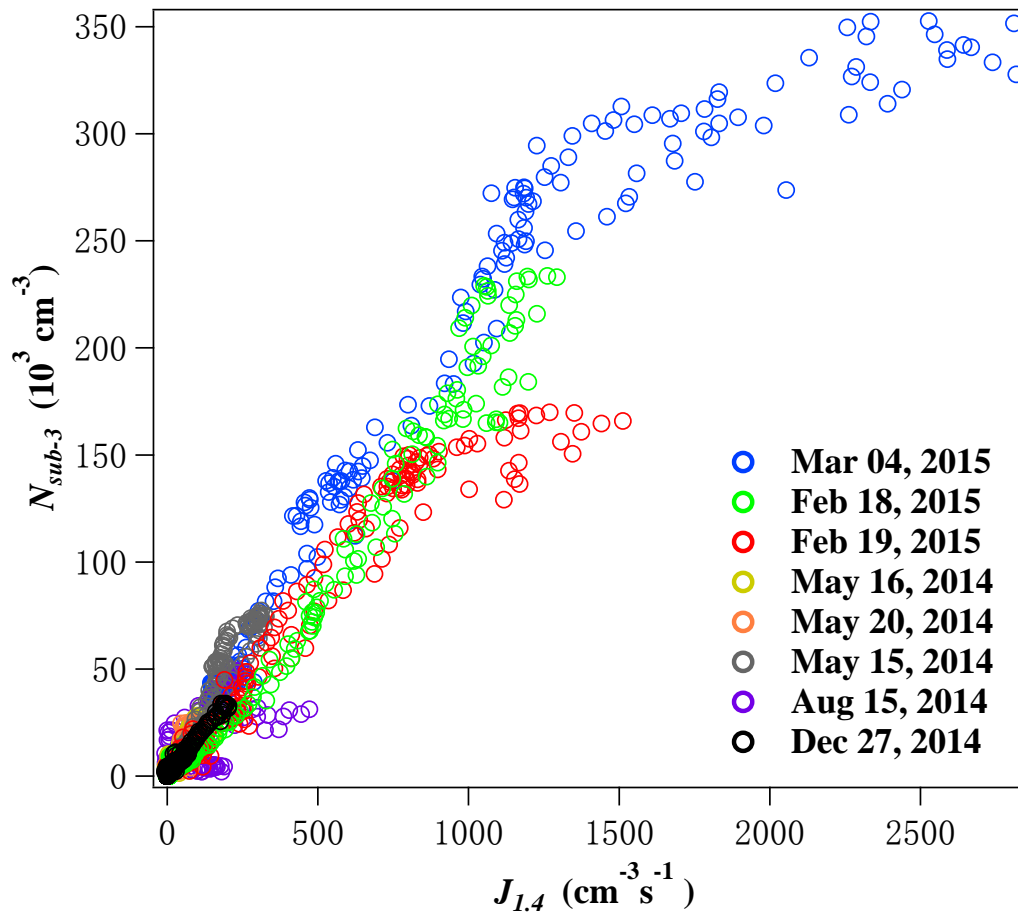
900

901

902

903

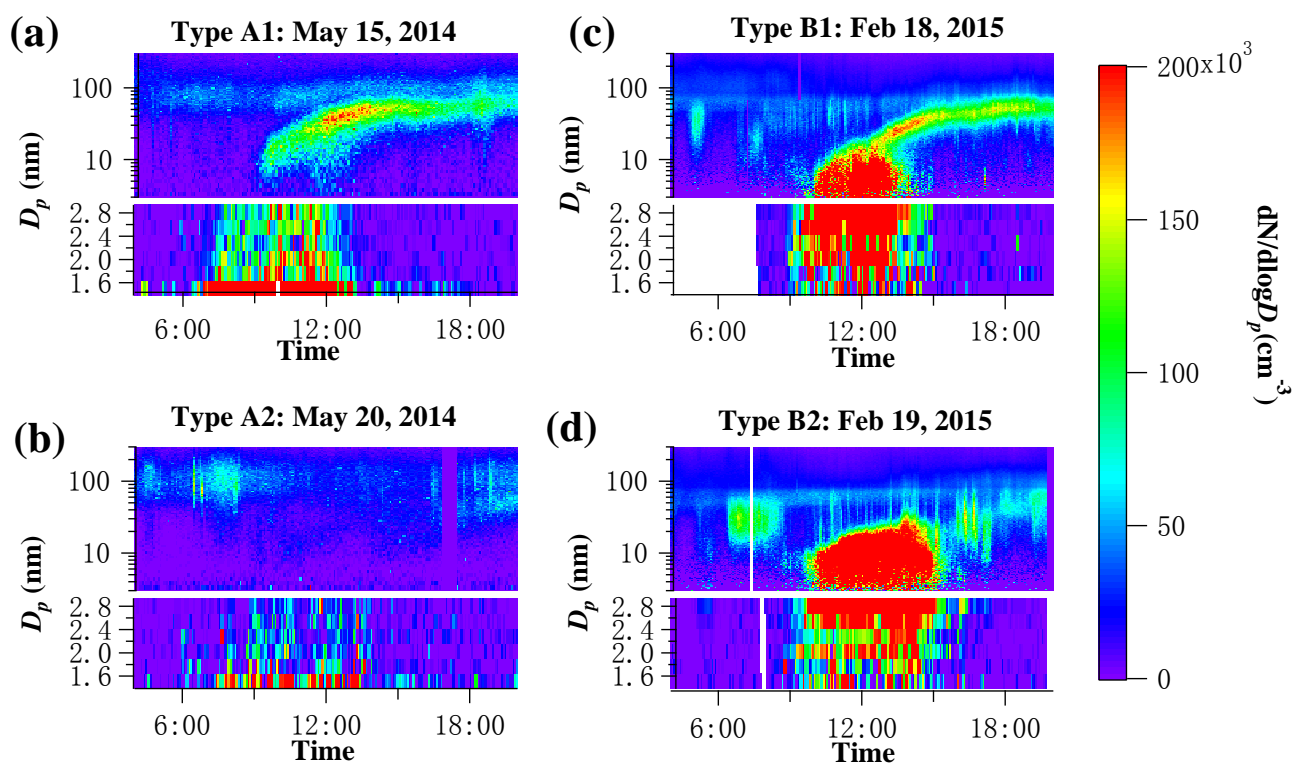
Figure 1. Locations of two urban measurement sites in Nanjing, the second largest megacity in the Yangtze River Delta region, China. ① is the NUIST site and ② is the summer measurement site.



905

906 Figure 2. N_{sub-3} vs. $J_{1.4}$ in the 8 nucleation events in February, May, December and August during
 907 2014-2015. The events were indicated by different colors (blue: March 1, 2015; green: February
 908 18, 2015; red: February 19, 2015; purple: August 15, 2014; black: December 27, 2014; grey:
 909 May 15, 2014; orange: May 20, 2014; yellow: May 16, 2014)

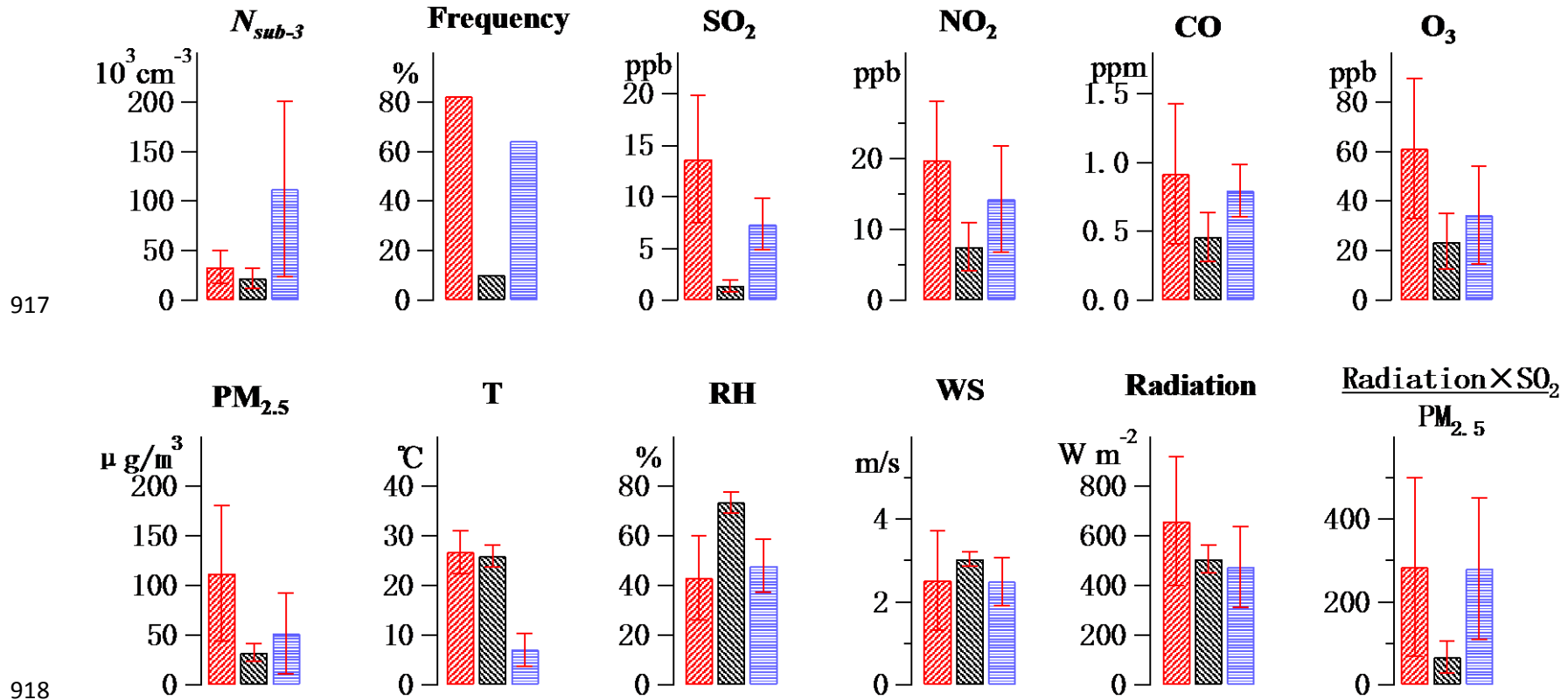
910



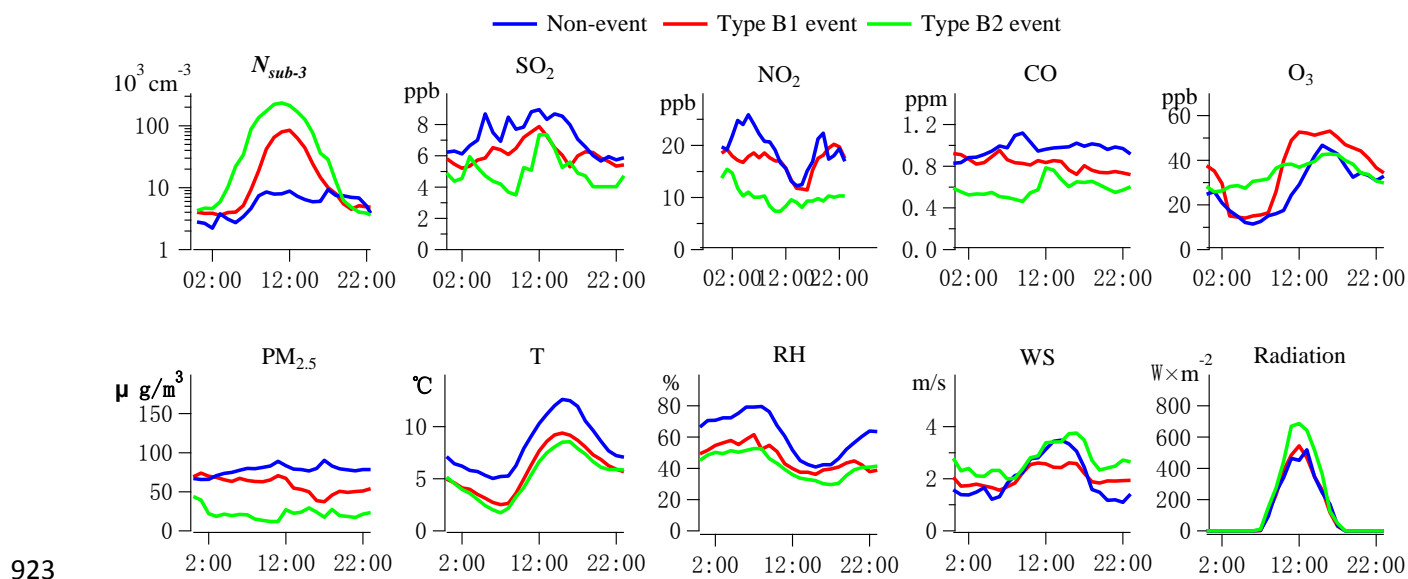
912

913 Figure 3. Size spectra of typical (a) Type A1 event on May 15, 2014; (b) Type A2 event on May 20,
 914 2014; (3) Type B1 event on February 18, 2015 and (d) Type B2 event on February 19, 2015 during
 915 our measurement period. Size spectra from 3-300 nm (logarithmic scale) and 1.4-3 nm (linear scale)
 916 were obtained using SMPS and nCNC, respectively.

Spring Summer Winter



917
918
919 Figure 4. Mean and standard deviation of event-averaged N_{sub-3} , anthropogenic trace gases (SO_2 , NO_2 , CO and O_3), $\text{PM}_{2.5}$, and meteorological
920 variables (temperature, RH, wind speed (WS), solar radiation, and radiation $\times \text{SO}_2 / \text{PM}_{2.5}$) for nucleation events in spring (n=17), summer (n=3)
921 and winter (n=14). Nucleation frequency (the percentage of event days out of total measurement days) was also shown.



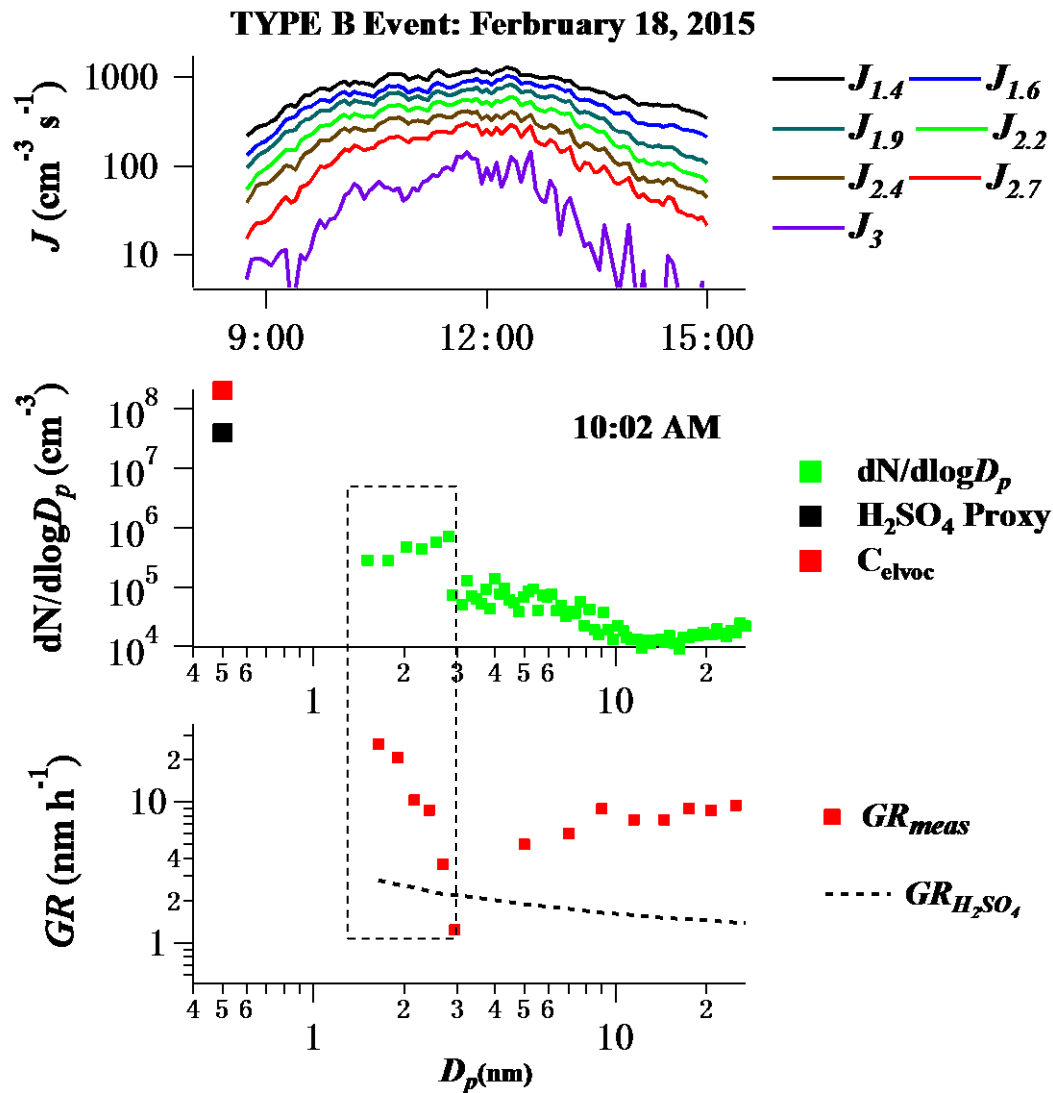
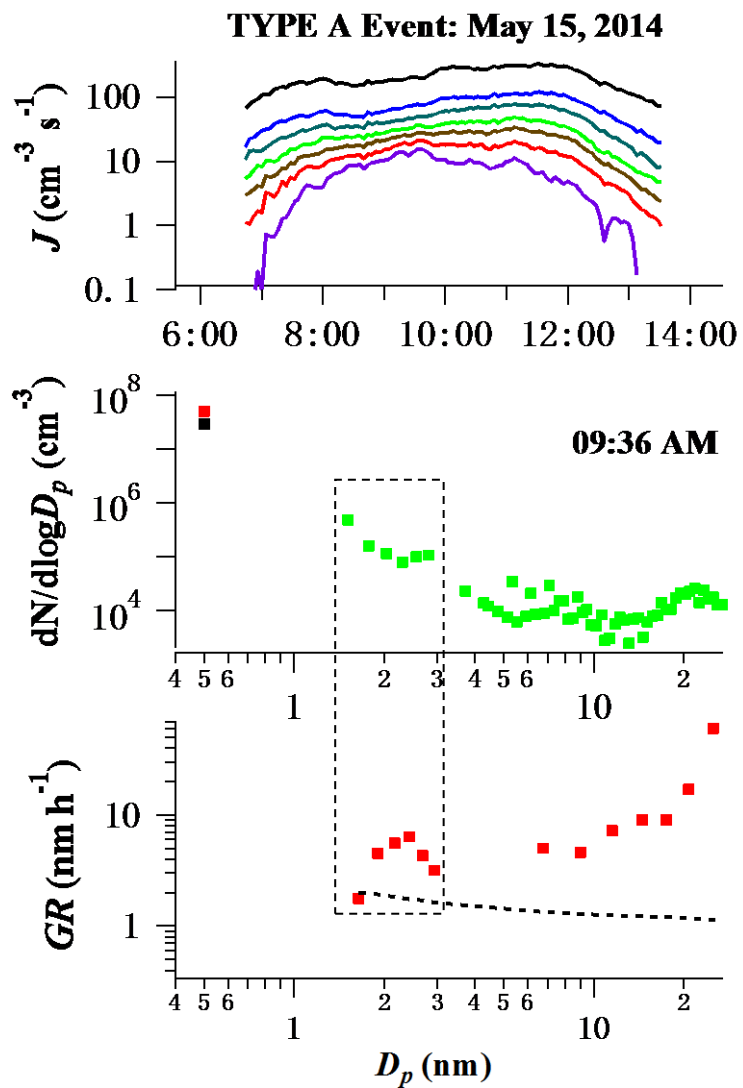
923

924 Figure 5. Diurnal variations of mean N_{sub-3} , anthropogenic trace gases (SO_2 , NO_2 , CO and O_3), $\text{PM}_{2.5}$,

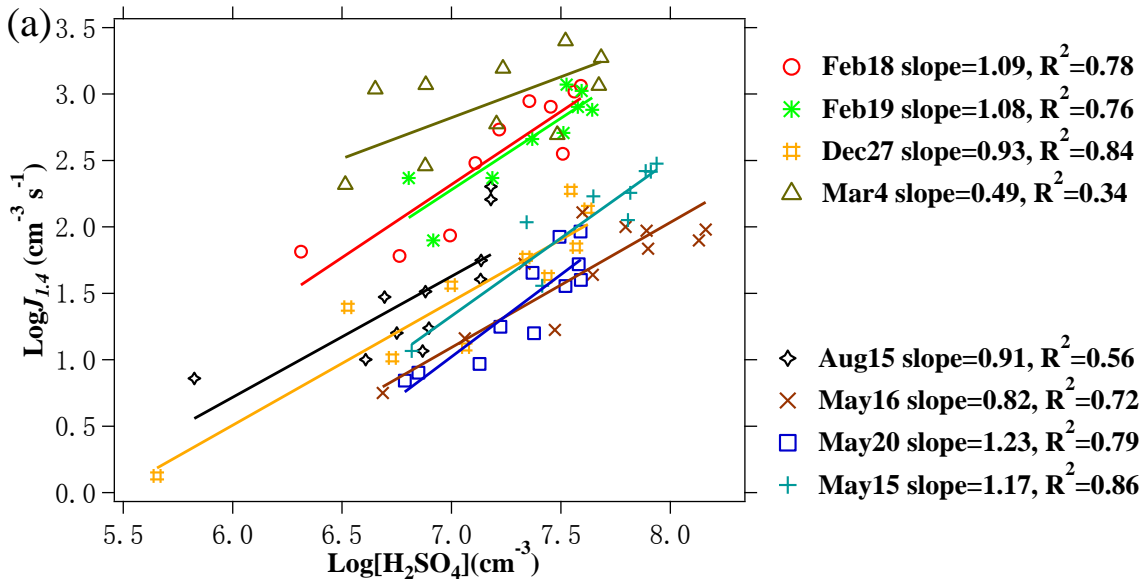
925 and meteorological variables (temperature, RH, wind speed, and solar radiation flux) on non-event

926 days (n=8, blue line) and event days (n=3 for Type B1 event, red line and n=6 for Type B2 event,

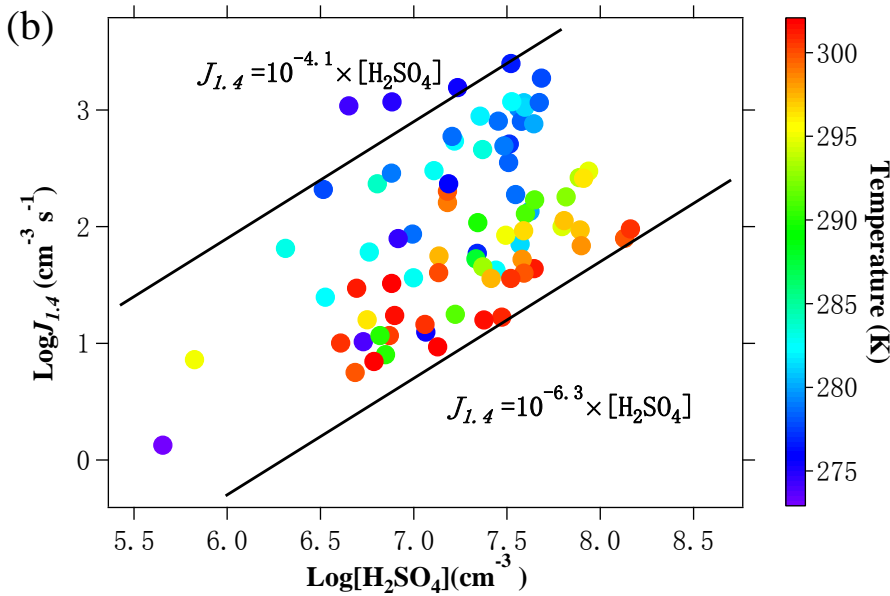
927 green line) during winter measurement period.



929 Figure 6. Upper: formation rates (or equivalently, particle growth fluxes) of 1.4, 1.6, 1.9, 2.2, 2.4, 2.7 and 3.0 nm cluster/particles on May 15
930 2014 (Type A1 event) and Feb 18 2015 (Type B1 event). Middle: particle size distribution ($dN/d\log D_p$, green square) selected during the two
931 events (9:36 AM and 10:02 AM). Lower: particle growth rates measured during the same time periods (GR_{meas} , red square). Also shown in the
932 figure were H_2SO_4 proxy (black square) and growth rates calculated from the H_2SO_4 proxy ($GR_{H_2SO_4}$, dashed black line), as well as the
933 calculated ELVOC concentration (C_{elvoc} , red square, see Eq.5) during the same time periods. Dashed boxes in the lower panels highlighted the
934 size distributions and growth rates between 1.4 and 3 nm measured with nCNC.

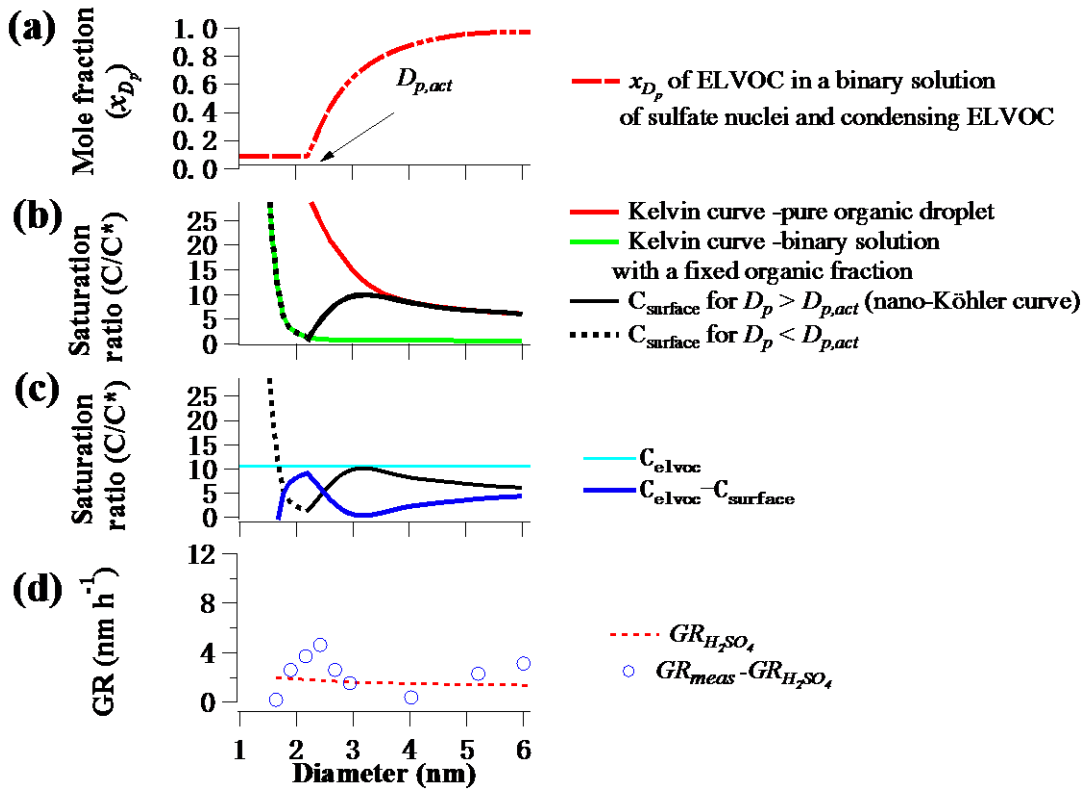


935



936

937 Figure 7. (a) Correlations between $\log J_{1.4}$ and $\log [H_2SO_4]$ for the 8 events. H_2SO_4 proxy was
 938 calculated according to Mikkonen et al. (2011). $J_{1.4}$ and $[H_2SO_4]$ were synchronized to 1 hour that
 939 was the time resolution of solar radiation data. The colored lines showed linear fits to the data of
 940 every single event. (b) The same dataset as (a), but with symbol color to indicate ambient
 941 temperature. Two black lines showed the linear dependences of $J_{1.4}=10^{-4.1} \times [H_2SO_4]$ and $J_{1.4}=10^{-6.3} \times$
 942 $[H_2SO_4]$, between which most of data points located.



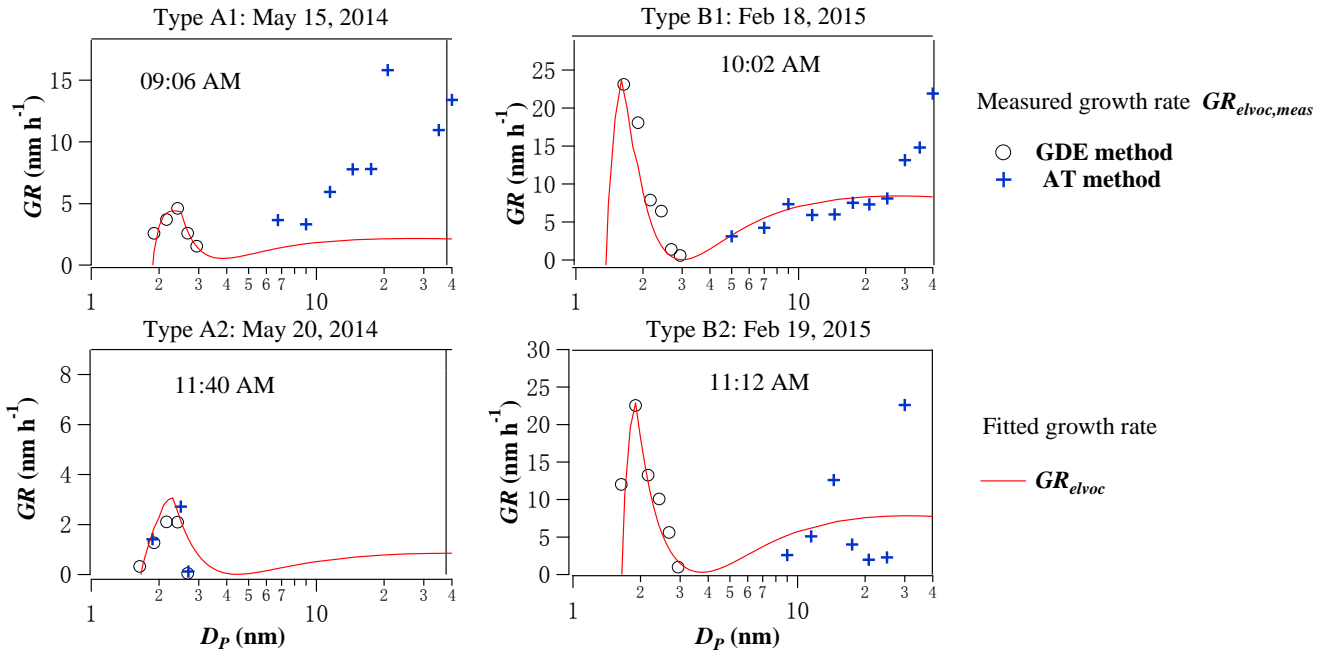
943

944 Figure 8. (a) Mole fraction of organics (x_{D_p}) in a binary solution of sulfate nuclei and activating
 945 organics (ELVOC) in a new particle. Nuclei activation diameter $D_{p,act}$ is the size where ELVOC
 946 begins to dilute the nuclei. (b) Kelvin equilibrium curves over a pure organic droplet (red line) and a
 947 binary solution with a fixed organic fraction (green line), nano Köhler curve for $D_p > D_{p,act}$ (black
 948 solid line) and surface concentration $C_{surface}$ for $D_p < D_{p,act}$ (black dashed line). (c) gas phase
 949 concentration of the organic vapor (C_{elvoc} , cyan line), surface concentration C_{∞} (black line), and
 950 $C_{elvoc} - C_{surface}$ (blue line). (d) Growth rate $GR_{H_2SO_4}$ due to H_2SO_4 (Mikkonen et al. 2011 proxy)
 951 and growth rate due to organic vapor $GR_{elvoc,meas}$, calculated as $GR_{meas} - GR_{H_2SO_4}$.

952

953

954



955

956

957 Figure 9. Comparisons of measured ($GR_{elvoc,meas}$, black circle) and fitted (GR_{elvoc} , red line) growth
 958 rates from Eq. (4) for typical Type A1, A2, B1, and B2 events. Also shown were growth rates
 959 calculated from appearance time method (blue cross) for sub-3 nm particles when growth rate was
 960 relatively small or for larger particles with large size intervals.

961